

AB INITIO INVESTIGATION OF THE NANOTRIBOLOGICAL PROPERTIES
OF THE H-BN/H-BN AND THE H-BN/Au(111) INTERFACES

A THESIS SUBMITTED TO
THE GRADUATE SCHOOL OF NATURAL AND APPLIED SCIENCES
OF
MIDDLE EAST TECHNICAL UNIVERSITY

BY

MERVE BAKSI

IN PARTIAL FULFILLMENT OF THE REQUIREMENTS
FOR
THE DEGREE OF MASTER OF SCIENCE
IN
PHYSICS

MAY 2019

Approval of the thesis:

**AB INITIO INVESTIGATION OF THE NANOTRIBOLOGICAL
PROPERTIES OF THE H-BN/H-BN AND THE H-BN/Au(111) INTERFACES**

submitted by **MERVE BAKSI** in partial fulfillment of the requirements for the degree
of **Master of Science in Physics Department, Middle East Technical University**
by,

Prof. Dr. Halil Kalıpcılar
Dean, Graduate School of **Natural and Applied Sciences**

Prof. Dr. Altuğ Özpıneci
Head of Department, **Physics**

Assoc. Prof. Dr. Hande Toffoli
Supervisor, **Physics, METU**

Prof. Dr. Oğuz Gülseren
Co-supervisor, **Physics, Bilkent University**

Examining Committee Members:

Assoc. Prof. Dr. Emre Taşcı
Physics Engineering, Hacettepe University

Assoc. Prof. Dr. Hande Toffoli
Physics, METU

Assist. Prof. Dr. Osman Barış Malcıoğlu
Physics, METU

Date:

I hereby declare that all information in this document has been obtained and presented in accordance with academic rules and ethical conduct. I also declare that, as required by these rules and conduct, I have fully cited and referenced all material and results that are not original to this work.

Name, Surname: Merve Baksi

Signature :

ABSTRACT

AB INITIO INVESTIGATION OF THE NANOTRIBOLOGICAL PROPERTIES OF THE H-BN/H-BN AND THE H-BN/Au(111) INTERFACES

Baksi, Merve

M.S., Department of Physics

Supervisor: Assoc. Prof. Dr. Hande Toffoli

Co-Supervisor : Prof. Dr. Oğuz Gülseren

May 2019, 77 pages

As the size of the systems reduces due to the advances in fabrication techniques, materials properties that apply at macroscopic scale start to lose their validity. As a reflection of this, friction at the atomic scale does not obey the macroscopic Da Vinci-Amontons' description. Each interface that experiences losses due to friction therefore requires a separate examination. A particularly intensely studied class of materials from a nanotribological point of view is the two-dimensional networks. In addition to the interface of two-dimensional materials with themselves, the interface between these materials and bulk surfaces are of interest. In this thesis, we examined the nanotribological properties of the h-BN/h-BN (hexagonal boron nitride), and h-BN/Au(111) surfaces using Density Functional Theory (DFT). h-BN/Au(111) interface is particularly relevant for modelling atomic force microscopy (AFM) and friction force microscopy (FFM) experiments since it is expected to reveal superlubric behaviour. We identify and discuss trends in the behavior of the friction force as a function of vertical load for experimentally feasible contact area. Moreover, in order to understand the edge effects of the interface, the interaction between small Au

clusters and the h-BN network is also investigated.

Keywords: nanotribology, h-BN, Au(111), Au clusters, vertical load, potential energy surface, friction coefficient

ÖZ

A-BN/A-BN VE A-BN/Au(111) YÜZEYLERİ ARASINDAKİ NANOTRİBOLOJİK ÖZELLİKLERİN İLK PRENSİP HESAPLARI İLE İNCELENMESİ

Baksi, Merve

Yüksek Lisans, Fizik Bölümü

Tez Yöneticisi: Doç. Dr. Hande Toffoli

Ortak Tez Yöneticisi : Prof. Dr. Oğuz Gülseren

Mayıs 2019 , 77 sayfa

Laboratuvar tekniklerindeki gelişmelerle birlikte, materyallerin boyutlarının küçülmesi, özelliklerinin de makroskopik boyuttakinden farklılaşmasına sebep olur. Bu kadar küçük boyutlarda, sürtünme kuvvetini tarif eden makroskopik Da Vinci-Amontons denklemleri geçerliliğini kaybeder. Bu sebeple nanotribolojik özellikleri incelenmek istenen her arayüzün özel olarak incelenmesi ve dikkate alınması gerekir. Bu anlamda çalışılan materyallerden iki boyutlu olanlar önemli bir yere sahiptir. Kendi aralarındaki etkileşimlerinin yanı sıra çeşitli kitle yüzeyleriyle de olan etkileşimleri önem taşımaktadır. Bu çalışmada, a-BN/a-BN (altıgensel boron nitrat) ve a-BN/Au(111) yüzeyleri arasındaki nanotribolojik özellikler yoğunluk fonksiyoneli teorisi (YFT) hesapları kullanılarak incelenmiştir. a-BN/Au(111) arayüzünün düşük sürtünmeli olması öngörüldüğü için özellikle atomik kuvvet mikroskobu ve sürtünme kuvveti mikroskobu deneylerinin modellenmesi açısından önem taşımaktadır. Bu çalışmada, a-BN/Au(111) arayüzündeki sürtünme kuvvetleri, değişik düşey yükler ve etki alanı altında çalışılmıştır. Buna ilave olarak, yüzeylerin uç etkilerini de gözlemleyebilmek

için Au topakları ile a-BN yüzeyi arasındaki etkileşim hesapları da yapılmıştır.

Anahtar Kelimeler: nanotriboloji, a-BN, Au(111), altın topakları, dikey yük, potansiyel enerji yüzeyi, sürtünme kuvveti katsayısı

To my family

ACKNOWLEDGMENTS

First and foremost, I am very grateful to my supervisor Assoc. Prof. Hande Toffoli for all the encouragement and endless support. Throughout this research, she has always motivated me with her wise and thoughtful comments and guided me to become a better researcher. I am very thankful to my co-supervisor Prof. Dr. Oğuz Gülseren who is always supportive and thoughtful as well. I cannot explain how happy I am that I am given the chance of working in this project with my both supervisors who are this knowledgeable and humble at the same time.

Moreover, I would like to thank the members of Computational Material Science Group for the nicest discussions about both science and life.

I am thankful to my love and best friend Sinan Yörükoğlu for his unconditional love and support. He always believed in me and was there for me when I needed.

Last but not least, I am very thankful to my family for always supporting me with my decisions and actions. I am very thankful to my dearest sisters, İrem Baksi and Yasemin Baksi, for being my best friends in the world and always supporting me.

This project is supported by the Scientific Research Council of Turkey (TÜBİTAK) via project code of 115F493.

TABLE OF CONTENTS

| | |
|---|------|
| ABSTRACT | v |
| ÖZ | vii |
| ACKNOWLEDGMENTS | x |
| TABLE OF CONTENTS | xi |
| LIST OF TABLES | xiii |
| LIST OF FIGURES | xiv |
| LIST OF ABBREVIATIONS | xix |
| CHAPTERS | |
| 1 INTRODUCTION | 1 |
| 1.1 Friction at the Atomic Level | 1 |
| 1.2 Simple Models of Friction | 5 |
| 2 METHODS AND CALCULATION DETAILS | 9 |
| 2.1 From the Many Body Schrödinger Equation to Density Functional Theory | 10 |
| 2.2 Preliminary Calculations for Hexagonal Boron Nitride (h-BN) | 18 |
| 2.3 Preliminary Calculations for Bulk Gold (Au) and Au clusters | 20 |
| 3 NANOTRIBOLOGICAL PROPERTIES OF THE TWO DIMENSIONAL HEXAGONAL BORON NITRIDE | 25 |
| 3.1 Friction Between Two h-BN Layers | 25 |

| | | |
|-------|--|----|
| 3.1.1 | Discussion | 30 |
| 3.2 | Friction Calculation Between Two h-BN Layers Under Applied Normal Force | 32 |
| 3.3 | Contact Area Decision for Load Force Calculations | 34 |
| 3.4 | Friction Calculation Between 3, 4 and 5 h-BN Layers | 42 |
| 4 | FRICITION INVESTIGATION OF AU(111) SURFACES AND GOLD CLUSTERS OVER TWO DIMENSIONAL HEXAGONAL BORON NITRIDE | 49 |
| 4.1 | Au(111)/h-BN Interface | 49 |
| 4.1.1 | 3 layered Au(111)/h-BN Interface: An Extreme Case Investigation | 50 |
| 4.1.2 | 4 layered Au(111)/h-BN Interface without the Strain | 52 |
| 4.2 | Nanotribological Properties of the Au(111)/h-BN Interface Under Applied Load Force | 56 |
| 4.3 | Gold Clusters and h-BN | 60 |
| 4.3.1 | Au atom over h-BN | 61 |
| 4.3.2 | Rhombic Au over h-BN | 61 |
| 4.3.3 | Icosahedral Au ₁₃ over h-BN | 64 |
| 5 | CONCLUSION AND DISCUSSION | 69 |
| | REFERENCES | 73 |

LIST OF TABLES

TABLES

| | | |
|-----------|--|----|
| Table 2.1 | Space vectors of icosahedron and cuboctahedron shaped gold clusters. | 23 |
| Table 3.1 | Average Friction Force between h-BN/h-BN for Different Sliding Directions | 32 |
| Table 3.2 | Friction coefficient and average friction force over the contact area at the h-BN/h-BN interface under applied load | 42 |
| Table 3.3 | Average Friction Force Change by the Number of Layers of the h-BN | 46 |
| Table 4.1 | Friction coefficient and average friction force between 4 layered Au(111) and h-BN. The results are shown with and without the contact area. | 59 |

LIST OF FIGURES

FIGURES

| | | |
|------------|--|----|
| Figure 1.1 | Illustration of real contact area at the asperities of an interface. Adapted from [22]. | 2 |
| Figure 1.2 | Atomic Force Microscopy. Adapted from [1]. | 4 |
| Figure 1.3 | Prandtl-Tomlinson model. Adapted from [25]. | 6 |
| Figure 1.4 | Frenkel-Kontorova model. Adapted from [25]. | 6 |
| Figure 1.5 | Frenkel-Kontorova-Tomlinson model. Adapted from [25]. | 7 |
| Figure 1.6 | Hybrid approach. Adapted from [25]. | 7 |
| Figure 2.1 | h-BN molecule | 19 |
| Figure 2.2 | Energy vs Cell Dimension Graph of BN molecule | 20 |
| Figure 2.3 | Effect of k-points on the lattice constant calculation of Au. | 21 |
| Figure 2.4 | Lattice constant optimization of gold (Au) with 12 k-points in each direction | 21 |
| Figure 2.5 | (111) surface representation. Adapted from [28]. | 22 |
| Figure 3.1 | Adhesion energy and friction force at the h-BN/h-BN interface in armchair (x) direction | 26 |
| Figure 3.2 | Honeycomb structure of BN | 27 |

| | | |
|-------------|--|----|
| Figure 3.3 | Above: Minimum point configuration of the two h-BN layers and the starting point of the motion. Left: two layers of BN at saddle point. Right: two layers of BN at AA stacking while sliding in armchair (x) direction. The atoms of the bottom h-BN layer are shown in relatively small sizes and pale colors compared to the atoms of the upper layer which are larger and have brighter colors. | 27 |
| Figure 3.4 | Adhesion energy and friction force of the h-BN/h-BN along armchair (x) direction | 28 |
| Figure 3.5 | Adhesion energy and friction force between the two h-BN along x-direction using the geometry optimization method at every point during the sliding. | 29 |
| Figure 3.6 | Two h-BN layers, upper layer is pulled through zigzag (y) direction. Above: The starting point of the sliding. | 30 |
| Figure 3.7 | Adhesion energy and friction force of the h-BN/h-BN along zigzag (y) direction | 30 |
| Figure 3.8 | Comparison of the h-BN/h-BN results | 31 |
| Figure 3.9 | Total Energy vs vertical distance at different lateral (x) positions at the interface of the h-BN/h-BN | 33 |
| Figure 3.10 | Load force vs vertical distance at different lateral positions (x) at the interface of h-BN/h-BN | 34 |
| Figure 3.11 | Friction force as a function of normal force for virgin $Si(111)$, SiO_2 coating and polished natural diamond. Measurements were made on a fresh $1\ \mu m \times 1\ \mu m$ scan areas using a diamond tip with a maximum force to (a) about $1300\ nN$ and (b) $40\ \mu N$ as cited from Leung and Goh's study [6] | 35 |
| Figure 3.12 | Change in friction force by contact area studied by Enachescu et al. [11] | 36 |

| | | |
|-------------|---|----|
| Figure 3.13 | Load Force vs vertical distance (z) over the contact area of $20,000 \text{ nm}^2$ | 37 |
| Figure 3.14 | Adhesion energy and friction force at the h-BN/h-BN interface under $100 \mu\text{N}$ load | 38 |
| Figure 3.15 | Adhesion energy and friction force at the h-BN/h-BN interface under $100 \mu\text{N}$ load with increased calculation steps | 39 |
| Figure 3.16 | Friction force between two BN sheets under several load forces . | 40 |
| Figure 3.17 | Top left: Upper BN is located at 1.0 \AA with respect to the initial configuration of AB-stacking. Top right: at 1.5 \AA . Bottom: at 3.0 \AA . . . | 41 |
| Figure 3.18 | Average charge density difference at the h-BN/h-BN interface . . | 41 |
| Figure 3.19 | Change in average friction force over the contact area and the friction coefficient change by the load. | 41 |
| Figure 3.20 | Three layered h-BN | 42 |
| Figure 3.21 | Adhesion energy and friction force at the interface of 3 layered h-BN/h-BN along x-direction | 43 |
| Figure 3.22 | Average friction force at the interface of 3 layered h-BN/h-BN . | 43 |
| Figure 3.23 | Four layered h-BN | 44 |
| Figure 3.24 | Adhesion energy and friction force at the interface of 4 layered h-BN/h-BN along x-direction | 44 |
| Figure 3.25 | Average friction force at the interface of 4 layered h-BN/h-BN . | 44 |
| Figure 3.26 | Five layered h-BN | 45 |
| Figure 3.27 | Adhesion energy and friction force at the interface of 5 layered h-BN/h-BN along x-direction | 45 |
| Figure 3.28 | Average friction force at the interface of 5 layered h-BN/h-BN . | 46 |
| Figure 3.29 | Average friction force vs number of h-BN layers | 46 |

| | | |
|-------------|--|----|
| Figure 4.1 | Left: (2×2) Au(111)- (2×2) BN when only Au(111) is contacted. Right: (2×2) Au(111)- (2×2) BN when only BN is extended. Pink color is for B atoms, blue is for N atoms and the yellow is for Au atoms where decreasing in size of the pale Au atoms indicates the relative distances from the uppermost h-BN. | 51 |
| Figure 4.2 | Adsorption energy at the interface of (2×2) Au(111)/ (2×2) h-BN. Left: when the h-BN is extended. Right: when the Au(111) is contracted. | 51 |
| Figure 4.3 | Adhesion energy and friction force at the interface of Au(111)/BN when BN is extended | 52 |
| Figure 4.4 | BN and Au(111) interface; unit cells are in perfect match. Pink, blue and yellow colors represent B, N and Au atoms respectively and the shrinking pale atoms is to represent the relative distance of the slab layers to the uppermost BN layer. | 53 |
| Figure 4.5 | Adhesion energy at the interface of 4 layered Au(111)/h-BN, when moved along x-direction for different z-distances | 54 |
| Figure 4.6 | Friction force at the interface of 4 layered Au(111)/h-BN, when moved along x-direction for different z-distances | 54 |
| Figure 4.7 | PES of 4 layered Au(111) and BN sheet. | 55 |
| Figure 4.8 | Relative positions during sliding as labeled on PES | 55 |
| Figure 4.9 | Adhesion energy as a function of separation distance between 4 layered Au(111) and BN at each lateral position | 56 |
| Figure 4.10 | Load as a function of separation distance between 4 layered Au(111) and BN at each lateral position over the estimated contact area | 57 |
| Figure 4.11 | Adhesion energy at the interface of 4 layered Au(111) and h-BN under several magnitudes of normal load | 58 |

| | | |
|-------------|---|----|
| Figure 4.12 | Friction force at the interface of 4 layered Au(111) and BN under applied normal force | 59 |
| Figure 4.13 | Average friction force and the friction coefficient as a function of load at the interface of 4 layered Au(111)/h-BN | 60 |
| Figure 4.14 | Average charge density difference at different lateral (x) position between Au(111) and h-BN | 60 |
| Figure 4.15 | Potential energy surface at the interface of Au atom and h-BN (right) along with the starting configuration (left). | 62 |
| Figure 4.16 | Adhesion Energy Graph of Au atom over (3x3)BN sheet | 62 |
| Figure 4.17 | Au ₄ is placed over (4 × 4) BN; top view and side view | 63 |
| Figure 4.18 | Au ₄ is placed over (4 × 4) BN when it is kept planar by force; top view and side view | 63 |
| Figure 4.19 | Au ₄ over (4x4)BN PES graphs; top: Tilted Au ₄ , bottom: Planar Au ₄ | 63 |
| Figure 4.20 | Adhesion energy and friction force of Rhombic Au (Au ₄) over BN (tilted configuration) | 64 |
| Figure 4.21 | Adhesion energy and friction force of Rhombic Au (Au ₄) over BN (planar configuration) | 64 |
| Figure 4.22 | Perfect icosahedral (top row) and perfect cuboctahedral (bottom row) from side and top view | 65 |
| Figure 4.23 | Structural transition from perfect icosahedral to distorted cuboctahedral when Au ₁₃ is placed over BN sample. | 66 |
| Figure 4.24 | Adhesion energy and friction force of icosahedral Au ₁₃ over h-BN | 67 |

LIST OF ABBREVIATIONS

Surface Forces Apparatus SFA
Atomic Force Microscopy AFM
Friction Force Microscopy FFM
Scanning Tunneling Microscope STM
Prandtl Tomlinson Model PT Model
Frenkel Kontorova Tomlinson Model FKT Model
Density Functional Theory DFT
Kohn-Sham KS
Local Density Approximation LDA
Generalized Gradient Approximation GGA
van der Waals vdW
van der Waals Density Functional vdW-DF
Lennard-Jones Potential LJ Potential
revised Perdew-Burke-Ernzerhof exchange functional revPBE
Gradient Expansion Approximation GEA
van der Waals Functional with Cooper correction vdW-DF-C09
Self Consistent Field SCF
Quantum Espresso QE
Potential Energy Surface PES

CHAPTER 1

INTRODUCTION

1.1 Friction at the Atomic Level

The behavior of particles at reduced scale are known to be very different especially when compared to the physics of the macro scale. Friction at the atomic level is no exception to this behavior and its driving mechanism has still not been understood completely. It is one of the most important physical phenomena which affects industry, scientific experiments and our daily lives. It should be eliminated in some cases in order to reduce the energy loss and hazardous emission caused by all moving mechanical systems regardless of their scale. As such, trying to reduce friction in engineering systems is of importance to preserve our limited energy sources and protect the planet [12].

Even though macroscopic sliding friction can be easily explained today by using Leonardo da Vinci's, Guillaume Amontons' and Augustin de Coulomb's discoveries made over hundreds of years ago, there is no generic set of equations to describe atomic-scale friction. Every surface interaction has to be examined individually since the atoms interact differently for different surfaces in contact. Depending on such system properties as the substances, layers, clusters behavior of friction forces present is expected to vary significantly.

There are several important points to be taken into account in the study of nanoscale friction. One that is worth mentioning is the difference in true and apparent contact area. The measurements taken in an experimental study using Surface Forces Apparatus (SFA) [25] revealed that when two surfaces touch each other, the contact takes place only at their asperities (unevenness of surface) and this shows that the true (mi-

croscopic) contact area is much less than the apparent (macroscopic) contact area. Thus, the friction is proportional not to the apparent contact area but the true contact area.

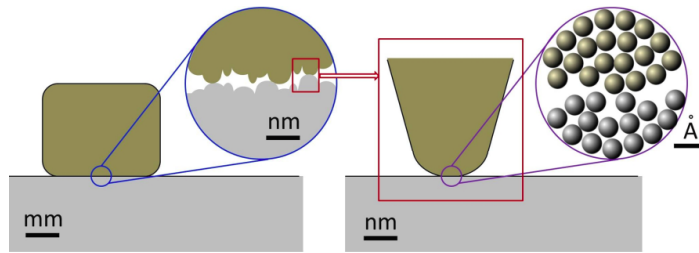


Figure 1.1: Illustration of real contact area at the asperities of an interface. Adapted from [22].

After Da Vinci (1452-1519) introduced the friction coefficient for the first time as the ratio of friction force to the normal load, French physicist Guillaume Amontons discovered the dependence of friction force to the normal load in 1699 and found also that the friction force does not depend on the contact area [5]. What is meant here is not the true contact area but the apparent one and the statement is in consistent with the SFA results as mentioned above. Hence, kinetic friction force is expressed as in Equation 1.1 and it implies that the friction force is proportional to the normal load, N , as well as it is independent of the apperant contact area.

Years later, another French physicist verified the previous findings of Da Vinci and Amontons, adding one more rule to the friction. The rule states that the friction does not depend on sliding velocity, v , once the motion starts [26]. However, this law does not hold at the nano scale.

The dependence of the friction force to the normal load is given by the following well-known equation.

$$F = \mu N \tag{1.1}$$

where μ is the friction coefficient in Equation 1.1.

Before going into the details, we present a simple model. This model involves two rigid walls are in contact. The lower wall, so called “substrate”, is fixed, and the upper wall is connected to a spring with stiffness constant, k , and pulled. If the spring

constant is large enough; one expects to have a smooth sliding as if it is pulled with a fixed sliding velocity by a rigid rod. On the other hand, if k is small, the system exhibits stick-slip motion. During the stick-slip motion, the upper wall (slider) gets stuck for a while and then suddenly proceeds its motion again.

This example shows that the friction force depends on the driving device, indicating that the harder the spring, the smaller the friction force. This effect is strong for the *commensurate* (if two crystals share common periodicity) surfaces since the atoms of commensurate surfaces can *lock* in during sliding. In order for the motion to proceed, all atoms that are locked must overcome the potential barrier in which they fall. On the other hand, friction is smaller for *incommensurate* surfaces since the atoms of the surfaces do not all lock at the same time during sliding. Therefore, the number of atoms that need to overcome the potential barrier in which they are located is less.

In addition, it is worth to mention a known fact that the lubricants reduce the wear and friction between two solids. This is correct for most of the macrotribological processes. Yet, unless strongly irreversible processes such as plastic deformation occurs, the presence of a few adsorbed lubricant particles can cause increase in solid friction by strengthening the surface corrugations and locking the two surfaces [36].

Some interfaces are known to exhibit extremely low friction coefficients, a phenomenon known as superlubricity. Superlubricity, which is driven entirely by surface properties, was first introduced by Motohisa Hirano and Kazumasa Shinjo in 1990s [18], [19]. In general, a system that has a friction coefficient of 0.01 and lower is called superlubric. Friction coefficient of two sliding surfaces of wood is 0.2 or larger and it can be larger than 1 for clean metal surfaces under dry conditions [33].

Superlubricity may be caused by several reasons classified accordingly as thermolubricity, quantum lubricity, liquid lubricity and structural lubricity [2]. In this thesis, the relevant mechanism of friction comes from the structural lubricity and is going to be elaborated in detail in the following chapters.

The experimental measurement of friction coefficients is very challenging. The most significant tools that help measure friction force are probe-based microscopes, namely, Atomic Force and Friction Force Microscopy (AFM/FFM). AFM designed based on

the Scanning Tunneling Microscope which can only make measurement for electrically conductive surfaces. Unlike STM, AFM can make measurements for both electrically conducting and insulating materials. They are capable of measuring the ultras-small forces even lower than $1 \mu N$. AFMs can both measure normal and lateral forces. They are called Friction Force Microscope or Lateral Force Microscope when they are modified to measure lateral forces or friction forces [5]. Over the past 30 years, nanotribological studies have accelerated and several interfaces are proven to be superlubric using different methods from experimental approaches to first-principle calculations. Li et al. [30] proved the superlubricity of lamellar molybdenite (MoS_2) by using in situ scanning electron microscopy and a silicon nanowire force sensor to sensitively measure friction forces and proved an earlier molecular dynamics study indicating that the friction coefficient of the system is less than 0.01 which is the upper limit for superlubric systems [37]. In this computational study, the rotational symmetry, hence the incommensurability of the system is the main reason for superlubric behavior.

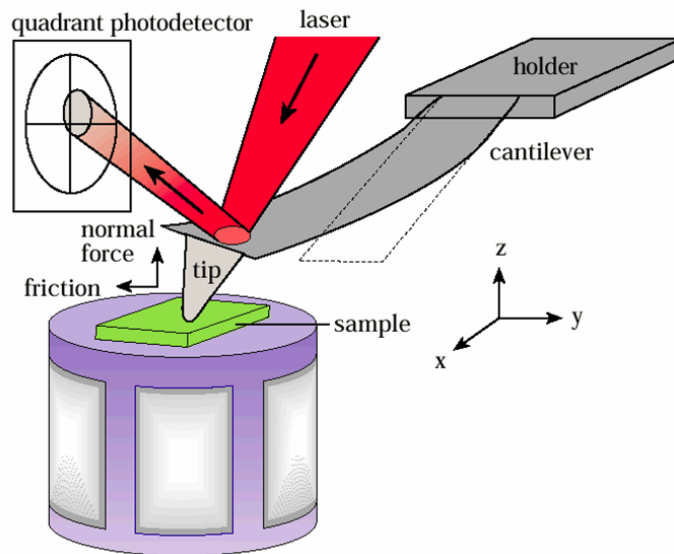


Figure 1.2: Atomic Force Microscopy. Adapted from [1].

In another study, conducted by Dienwiebel and his team [9], a lamellar material, graphite, was proved to be superlubric using a nanotribometer and at high vacuum. For the rotational angles that are not compatible with graphite’s six-fold symmetry, the system revealed ultra low friction force while at the exact commensurate cases

stick-slip motion has been observed.

In 2017, friction between graphene-graphene and graphene-h-BN interface have been investigated by Liu et al. [31] under high contact pressures by employing graphene-coated microsphere (GMS) probe. The friction coefficient of graphene-graphene interface reported as low as 0.025 and h-BN/graphene interface noted to be 0.0025 which proves the superlubric behavior of h-BN/graphene interface.

Many other research has been performed to reveal superlubricity especially using graphene, graphite flakes as well as other two-dimensional materials. In this thesis, h-BN/h-BN and Au(111)/h-BN interfaces have been modeled and investigated using first-principle calculations. The latter is modeled as a representative of gold coated AFM tip experiments. A couple of interfaces between gold clusters and h-BN have also been modeled in order to represent the atomically sharp AFM tips and to see the edge effects of the tips .

1.2 Simple Models of Friction

In attempt to understand atomic-scale friction, several models have been developed in the past decades. Here, we present them in chronological order.

Prandtl-Tomlinson model of atomic friction which was established by Prandtl in 1928 and Tomlinson in 1929, is the first model which helps us understand wearless atomic level friction. In this model, two materials are placed over one another and are in relative motion with respect to each other. The lower layer can be set in rest so that it represents a periodic potential to the sliding upper layer. The surface atoms on the upper layer are connected to the rest of the atoms in the material with springs as a representative of chemical bonds while the surface atoms are not connected to each other (Figure 1.3). Because of this, Prandtl-Tomlinson model is also known as independent oscillator. During motion, springs will oscillate and there will be mechanical vibrations which are called phonons. Phonons are the responsible mechanism to the energy dissipation.

In this picture, oscillators move either in a slow and smooth motion or will perform

abrupt jumps from one position to another depending on the spring constant, k , which is the interaction forces exhibit within the materials as well as the sliding velocity and the size of the potential barrier shown in Equation 1.2. During sliding, surface atoms of the upper layer can lock in depending on these parameters and they can only continue their motion when they have enough energy to overcome the potential barrier in which they fall. The abrupt jumps cause stick-slip motion where continuous sliding can be observed for small sliding velocities, stiff springs and small potentials.

$$m\ddot{x} = k(v_0t - x) - \eta\dot{x} - N\sin(2\pi x/a) \tag{1.2}$$

where m is the mass of the particle, N is the amplitude of the periodic potential, which is created by the still substrate, v_0 is the sliding velocity of the mobile layer, η is the damping coefficient. Since η is the factor related to the phonon dissipation energy, one cannot talk about friction without η term in a high enough temperature.

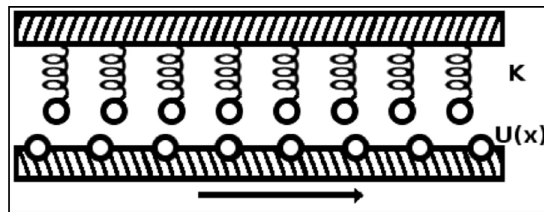


Figure 1.3: Prandtl-Tomlinson model. Adapted from [25].

Frenkel-Kontorova model is another representative model which helps us apprehend the atomic friction force. In this model, surface atoms are connected to each other by a spring different than the case in Prandtl-Tomlinson model. In addition, surface atoms are not connected to the rest of the solid. Figure 1.4 shows the model.

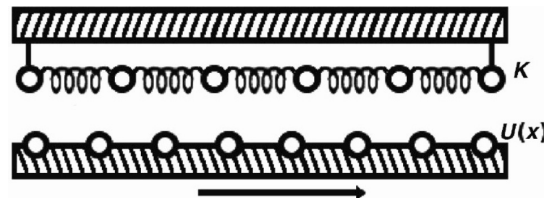


Figure 1.4: Frenkel-Kontorova model. Adapted from [25].

Another representation of atomic friction is Frenkel-Kontorova-Tomlinson Model. In FKT model, surface atoms are both connected to the each other and to the rest of the upper solid by the springs. See Figure 1.5.

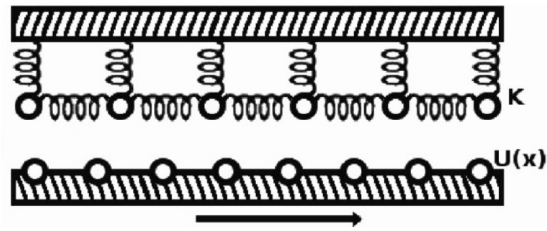


Figure 1.5: Frenkel-Kontorova-Tomlinson model. Adapted from [25].

There is hybrid approach for understanding atomic friction which is more complicated than the previous models. In this model of hybrid approach, all atoms in the solid are assumed to be connected to each other by vertical and horizontal springs as it is seen in Figure 1.6. This may seem to be the most accurate model to represent a real system, however, one does not need to take the farthestmost interactions between atoms into account since especially for the bulk materials the atoms other than the surface atoms have no contribution to the friction during the motion owing to the stability of the material, i.e; in the case of wearless friction. Therefore, hybrid approach reduces itself to the previous models by nature.

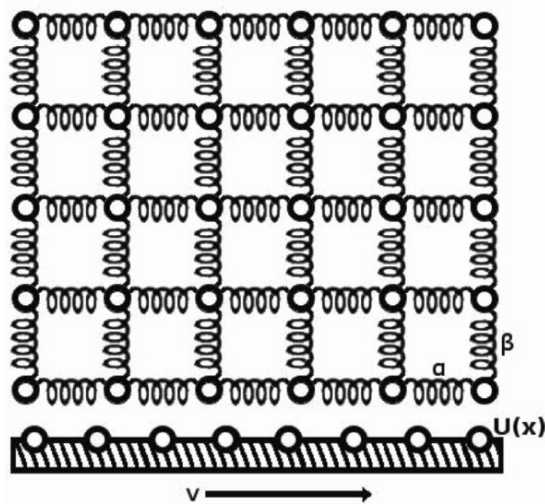


Figure 1.6: Hybrid approach. Adapted from [25].

CHAPTER 2

METHODS AND CALCULATION DETAILS

An accurate description of the electronic and structural properties of many-body systems is of crucial importance for the advent of materials science. The central paradigm in theoretical calculations is that the properties of a quantum mechanical system is defined by the Schrödinger equation. However, this picture is complicated since the many-electron system is in principle has $3N$ degrees of freedom where N is the number of quasiparticles in the system. At this point Density Functional Theory (DFT) provides an innovative method and simplifies many-electron systems in a very elegant way. To put it concisely, DFT is an ab-initio simulation technique that uses the electron density in order to analyze the properties of many-body systems.

The solution process starts with the construction of the Hamiltonian of the many-electron system. In Equation 2.1, the first term is the kinetic energy of the nucleus, the second one is the nucleus-nucleus interaction potential, the third one is the kinetic energy of the electrons, the fourth is the electron-electron interactions and the fifth term is the nucleus-electron interaction potential.

$$\begin{aligned}\hat{H} &= \hat{T}_n + \hat{V}_{n-n} + \hat{T}_e + \hat{V}_{n-e} + \hat{V}_{e-e} \\ &= -\frac{\hbar^2}{2m_I} \sum_I^{N_n} \nabla_I^2 + \frac{e^2}{4\pi\epsilon} \frac{1}{2} \sum_{I \neq J} \frac{Z_I Z_J}{|\vec{R}_I - \vec{R}_J|} - \frac{\hbar^2}{2m_e} \sum_i^N \nabla_i^2 \\ &\quad - \frac{e^2}{4\pi\epsilon} \sum_I^{N_{ion}} \sum_i^{N_e} \frac{Z_I}{|\vec{r}_i - \vec{R}_I|} + \frac{1}{2} \frac{e^2}{4\pi\epsilon} \sum_{i \neq j}^N \frac{1}{|\vec{r}_i - \vec{r}_j|}\end{aligned}\tag{2.1}$$

In Equation 2.1 \vec{r}_i and \vec{r}_j define the locations of the i^{th} and the j^{th} electrons respectively whereas \vec{R}_I is the location of the \vec{R}_I^{th} nucleus. The Born-Oppenheimer approximation states that the kinetic energy of the nucleus is negligible compared to the electrons since the nucleus is much heavier than an electron. However, one should keep in mind that it is only for practical reasons, since nuclei cannot be perfectly immobile in order to satisfy uncertainty principle; $\Delta x \Delta p \geq \hbar$ [16]. Also, the nucleus-nucleus interaction potential, \hat{V}_{n-n} can be omitted from the expression since it is a constant value and can be calculated easily. Then, Equation 2.1 is decoupled

$$\hat{H} = \hat{T}_e + \hat{V}_{e-e} + \hat{V}_{n-e} \quad (2.2)$$

The early wavefunction-based methods such as the Hartree and the Hartree-Fock methods [34] rely on the construction of many-body wave functions from single-particle orbitals. Whereas the wavefunction is constructed as a simple product in the Hartree method, Slater determinants are employed in the Hartree-Fock method. The problem is then solved in a variational manner employing a suitable basis set to describe the orbitals. While straightforward, neither of these methods capture the important correlation effects and therefore have limited use for our purposes.

In 1964, Hohenberg and Kohn have been developed a more sophisticated method called *Density Functional Theory (DFT)* [20] which earned Walter Kohn a Nobel Prize in Chemistry, thirty four years later in 1998. This innovative method relies on the description of the ground state energy as a functional of the electronic density, which, through two simple yet elegant theorems proposed by Hohenberg and Kohn, can be minimized to obtain the ground state density. A brief account of the details will be presented in the following sections.

2.1 From the Many Body Schrödinger Equation to Density Functional Theory

The electronic density operator is a measure of the contribution from each electron to the probability of finding electrons at point \vec{r} .

$$\hat{n}(\vec{r}) = \sum_i^N \delta(\vec{r} - \vec{r}_i) \quad (2.3)$$

where $i = 1, 2, 3, \dots, N$ is the electron index. The expectation value of the density operator yields the electron density through the following derivation :

$$\begin{aligned} \langle \hat{n}(\vec{r}) \rangle &= \langle \Psi | \hat{n}(\vec{r}) | \Psi \rangle = \int \Psi^*(\vec{r}_1, \vec{r}_2, \dots, \vec{r}_N) \sum_i^N \delta(\vec{r} - \vec{r}_i) \Psi(\vec{r}_1, \vec{r}_2, \dots, \vec{r}_N) d\vec{r}_1 d\vec{r}_2 \dots d\vec{r}_N \\ &= \int |\Psi(\vec{r}, \vec{r}_2, \dots, \vec{r}_N)|^2 d\vec{r}_2 d\vec{r}_3 \dots d\vec{r}_N + \int |\Psi(\vec{r}_1, \vec{r}_3, \dots, \vec{r}_N)|^2 d\vec{r}_1 d\vec{r}_3 \dots d\vec{r}_N + \dots \\ &= N \int |\Psi(\vec{r}_1, \vec{r}_2, \dots, \vec{r}_N)|^2 d\vec{r}_1 d\vec{r}_2 \dots d\vec{r}_N \end{aligned} \quad (2.4)$$

One should note that once the Equation 2.4 is integrated over all space, the total number of electrons, N , is obtained using the fact that wavefunction is normalizable.

$$\int n(\vec{r}) d\vec{r} = N \quad (2.5)$$

We remind the reader that the total energy takes the following form from Equation 2.2 in atomic units.

$$\hat{H}_e = \hat{T}_e + \hat{V}_{n-e} + \hat{V}_{e-e} = -\frac{1}{2} \sum_i^N \nabla_i^2 + \sum_I^{N_{ion}} \sum_i^{N_e} v_{ext}^I(\vec{r}_i) + \frac{1}{2} \sum_{i \neq j}^N \frac{1}{|\vec{r}_i - \vec{r}_j|} \quad (2.6)$$

To utilize the density, we start with the external potential, which can be written exactly in terms of the single particle density.

$$\hat{V}_{ext} = \sum_i^N v_{ext}^I(\vec{r}_i) \quad (2.7)$$

The corresponding expectation value is

$$E_{ext} = \int \Psi^*(\vec{r}_1, \dots, \vec{r}_N) \left(\sum_i^N v_{ext}^I(\vec{r}_i) \right) \Psi(\vec{r}_1, \dots, \vec{r}_N) d\vec{r}_1 d\vec{r}_2 \dots d\vec{r}_N \quad (2.8)$$

After some manipulations, Equation 2.8 becomes

$$\begin{aligned}
&= \int v_{ext}(\vec{r}_1) \left[\int |\Psi(\vec{r}_1, \dots, \vec{r}_N)|^2 d\vec{r}_2 d\vec{r}_3 \dots d\vec{r}_N \right] d\vec{r}_1 \\
&+ \int v_{ext}(\vec{r}_2) \left[\int |\Psi(\vec{r}_1, \dots, \vec{r}_N)|^2 d\vec{r}_1 d\vec{r}_3 \dots d\vec{r}_N \right] d\vec{r}_2 + \dots + \dots
\end{aligned} \tag{2.9}$$

Realizing that all integrals yield the same expression, we finally obtain

$$E_{ext} = \int n(\vec{r}) v_{ext}(\vec{r}) d\vec{r} \tag{2.10}$$

The electron-electron interaction in the Hamiltonian is complicated due to the correlation between all electrons.

$$\hat{V}_{e-e} = \frac{1}{2} \sum_{i \neq j} \frac{1}{|\vec{r}_i - \vec{r}_j|} \equiv \frac{1}{2} \sum_{i \neq j} v_{e-e}(\vec{r}_i, \vec{r}_j) \tag{2.11}$$

Then, the expectation value of \hat{V}_{e-e} is going to be E_{e-e} and can be found as follows.

$$E_{e-e} = \int \Psi^*(\vec{r}_1, \vec{r}_2, \dots, \vec{r}_N) \hat{V}_{e-e} \Psi(\vec{r}_1, \vec{r}_2, \dots, \vec{r}_N) d\vec{r}_1 d\vec{r}_2 \dots d\vec{r}_N \tag{2.12}$$

Substituting Equation 2.11 into Equation 2.12, we will have $N(N - 1)$ non-distinct pairs in the sum and notice that all terms are the same. Therefore, we have:

$$E_{e-e} = \int v_{e-e}(\vec{r}, \vec{r}') d\vec{r}, d\vec{r}' \left[\frac{N(N - 1)}{2} \int |\Psi(\vec{r}, \vec{r}', \vec{r}_3, \dots, \vec{r}_N)|^2 d\vec{r}_3 d\vec{r}_4 \dots d\vec{r}_N \right] \tag{2.13}$$

Here, the term inside the square brackets is defined as the two-particle density.

$$n^{(2)}(\vec{r}, \vec{r}') = \left[\frac{N(N - 1)}{2} \int |\Psi(\vec{r}, \vec{r}', \vec{r}_3, \dots, \vec{r}_N)|^2 d\vec{r}_3 d\vec{r}_4 \dots d\vec{r}_N \right] \tag{2.14}$$

Finally, we have the electron-electron interaction term in the Hamiltonian as a function of density as we desire.

$$E_{e-e} = \int v_{e-e}(\vec{r}, \vec{r}') n^{(2)}(\vec{r}, \vec{r}') d\vec{r}, d\vec{r}' \quad (2.15)$$

The electron density, as described above, is derived from a single-particle operator. Therefore, in preparation of an approximation to reduce the two-particle density to a single-particle density, we separate it into an uncorrelated contribution and the remaining correlation. In crystals and systems generally relevant for materials science, this contribution is crucial yet small in magnitude.

$$n^{(2)}(\vec{r}, \vec{r}') = \frac{n(\vec{r})n(\vec{r}')}{2} + \Delta n^2(\vec{r}, \vec{r}') \quad (2.16)$$

Next, using the above formulation, E_{e-e} becomes

$$E_{e-e} = \frac{1}{2} \int \frac{n(\vec{r})n(\vec{r}')}{|\vec{r} - \vec{r}'|} d\vec{r}d\vec{r}' + \int \frac{\Delta n^2(\vec{r}, \vec{r}')}{|\vec{r} - \vec{r}'|} d\vec{r}d\vec{r}' \quad (2.17)$$

In Equation 2.17, the first term is the classical potential of a continuous charge distribution and is called Hartree energy, E_H . In a more compact form, it will be as in Equation 2.18.

$$E_{e-e} = E_H + \Delta E_{e-e} \quad (2.18)$$

The kinetic energy operator cannot simply be manipulated in terms of the density functional theory as was done for the other terms, since it involves a derivative operator. To explain the workaround usually employed, we introduce the Hohenberg-Kohn theorems.

Hohenberg and Kohn's first theorem states that there is a one-to-one correspondence between the ground state density of a system and the external potential. This allows for the unique determination of the ground state density [20].

Hohenberg and Kohn's second theorem states that a universal functional of energy can be defined in terms of density, and the minimum of this functional is the exact ground state energy of the system [20].

$$\frac{\delta E}{\delta n} = 0 \quad (2.19)$$

However, we can only take the derivative of E_H in the total energy since the kinetic energy and the correlation energy terms cannot be differentiated with respect to density in their current forms. The need for a single-particle operator is met by the Kohn-Sham ansatz.

According to Kohn-Sham ansatz, for each N-particle system, it is possible to find an auxiliary system of non-interacting particles such that the exact ground state density is identical to the true system at hand [24]. Since the particles in the auxiliary system are independent, the electronic density reduces to

$$n(\vec{r}) = \sum_{i=1}^{N_e} |\Phi_i(\vec{r})|^2 \quad (2.20)$$

where $\Phi_i(\vec{r})$ are unspecified single-particle orbitals.

Now, instead of differentiating total energy with respect to density, which is not possible due to the kinetic energy term, it is possible to differentiate it with respect to the complex conjugate of the single-particle orbital, i.e. instead of $\frac{\delta E}{\delta n}$ one should consider $\frac{\delta E}{\delta \Phi_i^*}$.

$$\frac{\delta E}{\delta \Phi_i^*} = \frac{\delta E}{\delta n} \frac{\delta n}{\delta \Phi_i^*} = \frac{\delta E}{\delta n} \Phi_i \quad (2.21)$$

where we use the following relation to simplify it.

$$n(\vec{r}) = \sum_i |\Phi_i(\vec{r})|^2 = \sum_i \Phi_i^* \Phi_i \quad \frac{\delta n}{\delta \Phi_i^*} = \Phi_i \quad (2.22)$$

Thus, if $\frac{\delta E}{\delta n} = 0$, so is $\frac{\delta E}{\delta \Phi_i^*}$. This time though, there are N-equations to be solved.

Now that the single-particle definition of the ground state density is established, one is able to differentiate the kinetic energy noting that the kinetic energy in terms of single-particle orbitals is actually not equal to the real kinetic energy of the system. This is

because it is the kinetic energy of the auxiliary system and ignores the correlation between the electrons.

$$T_{KS} = -\frac{1}{2} \sum_{i=1}^{N_e} \int \Phi_i^*(\vec{r}) \nabla^2 \Phi_i(\vec{r}) d\vec{r} \quad T_{true} = T_{KS} + \Delta T \quad (2.23)$$

where T_{KS} is the single-particle kinetic energy of the auxiliary system and ΔT comes from the correlation in the real system.

Differentiating of the single-particle kinetic energy as shown in Equation 2.23 then yields

$$\frac{\delta T_{KS}}{\delta \Phi_i^*} = -\frac{1}{2} \nabla^2 \Phi_i(\vec{r}) \quad (2.24)$$

Using Equation 2.10 and performing the differentiation of the E_{ext} will yield:

$$\frac{\delta E_{ext}}{\delta \Phi_i^*} = v_{ext}(\vec{r}) \Phi_i(\vec{r}) \quad (2.25)$$

The remaining term to be differentiated is the E_{e-e} as defined in Equation 2.17, where the result is:

$$\frac{\delta E_{e-e}}{\delta \Phi_i^*} = \frac{\delta(E_H + \Delta E_{e-e})}{\delta \Phi_i^*} \quad (2.26)$$

The exact form of ΔE_{e-e} is not known but it is possible to perform the differentiation of the first term in Equation 2.26.

$$\frac{\delta E_H}{\delta \Phi_i^*} = \int \frac{n(\vec{r}')}{|\vec{r} - \vec{r}'|} d\vec{r}' \Phi_i^* \quad (2.27)$$

The unknown terms in the energy are added up and called as exchange-correlation energy, E_{xc} , in Equation 2.28

$$E_{xc} = \Delta E_{e-e} + \Delta T \quad (2.28)$$

With the definitions and the differentiations of all the terms in the total energy, one arrives at the following:

$$\frac{\delta E_{total}}{\delta \Phi_i^*} = -\frac{1}{2}\nabla^2\Phi_i(\vec{r}) + v_{ext}(\vec{r})\Phi_i(\vec{r}) + \int \frac{n(\vec{r}')}{|\vec{r}' - \vec{r}|}d\vec{r}'\Phi_i + \frac{\delta E_{xc}}{\delta \Phi_i^*} \quad (2.29)$$

During minimization of the total energy, the orthonormality of the Kohn-Sham orbitals must be maintained. This is achieved by the introduction of a set of Lagrange multipliers. At the end of the minimization following equation is obtained:

$$[\hat{T} + \hat{V}_{ext} + \hat{V}_H + \hat{V}_{xc}]\Phi_i = \epsilon_i\Phi_i \quad (2.30)$$

The total term in the parantheses of Equation 2.30 is called the Kohn-Sham Hamiltonian, \hat{H}_{KS} , and the eigenvalues, ϵ_i , are referred to the Kohn-Sham energies.

So far exact, the operator in Equation 2.30 is still a two-particle operator and can therefore not be solved practically using a single-particle density. A very active and rich field has emerged since the early work of Kohn, Hohenberg and Sham that has explored accurate approximations under the common name of exchange-correlation functionals.

Commonly used functionals to evaluate exchange-correlation energy are local-density approximation (LDA) and generalized gradient approximation (GGA) [23, 39]. LDA depends merely on density variable whereas GGA includes the gradient of the density as well. Although accurate for covalently bonded systems, these local and semilocal functionals do not involve the long-range, non-local correlations which are the base of vdW interactions. vdW interactions embrace all possible forces between molecules including permanent dipole-dipole, permanent dipole-induced dipole and two instantaneously induced dipoles which is also known as London dispersion force [3, 32]. The classical, non-dispersive part of the vdW is already included in DFT but long-range dispersion corrections are needed to be implemented separately to the $E_{xc}[n]$ in order especially to model accurately the systems that have polar nature such as h-BN that we have examined in this thesis.

The simplest known vdW forces are described in the form of Lennard-Jones potential,

$V_{LJ}(\vec{r}) = 4\epsilon\left[\left(\frac{\sigma}{r}\right)^{12} - \left(\frac{\sigma}{r}\right)^6\right]$, where the first term is the short-range Pauli repulsion forces and the second term is the long-range attractive dispersion forces, i.e. London dispersion forces. Here, ϵ is the bond energy defined as the energy necessary to bring particles to make a bond or the depth of the potential whereas σ is the distance at which the intermolecular potential between the two particles is zero. The second term of LJ potential commonly referred to as vdW forces in condensed matter community and can be implemented to DFT empirically. Although it can be added to DFT in order to improve the formalization of the dispersion, the search for a better correction to an exchange-correlation energy has been an ongoing research due to the limitations of LJ potential including that it is proper only for systems consisting of neutral atoms and that it does not contain density so that it can be implemented analytically to the theory.

A promising solution lies in the non-local correlation functional of the Rutgers-Chalmers collaboration named vdW density functional (vdW-DF), where long-range dispersion effects are implemented as a perturbation to the LDA correlation term [45]. vdW-DF tackles the non-local vdW interaction by an approximate non-empirical method.

$$E_{xc}^{vdW-DF}[n] = E_x^{revPBE}[n] + E_c^{LDA}[n] + E_c^{nl}[n] \quad (2.31)$$

The first term is the revised Perdew-Burke-Ernzerhof (revPBE) exchange functional, which is a generalized gradient correction and together with the second term of LDA correlation they are semi-local. The last term in Equation 2.31 concerns only the correlation, and vdW interaction belongs to this part. However, one should remember that the total exchange-correlation potential includes the parts arising from $E_x^{revPBE}[n]$ and $E_c^{LDA}[n]$ as well.

$$E_x^{GGA}[n] = \int d^3(\vec{r}) n(\vec{r}) \epsilon_x^{hom}(n) F_x(s) \quad (2.32)$$

In Equation 2.32, $\epsilon_x^{hom}(n) = -3ek_F/4\pi$ is the energy per particle in a homogeneous gas with $k_F = (3\pi^2n)^{1/3}$, whereas $F_x(s)$ is the enhancement factor which is a function of the density and its gradient, $F_x(s) = |\nabla n|/(2k_F n)$. The choice of $F_x(s) = 1$ gives the LDA exchange. Further designation has been performed by

Cooper et al. and vdW-DF-C09 functional has been developed with the choice of $F_x(s) = 1 + \mu s^2 e^{-\alpha s^2} + \kappa(1 - e^{-\alpha s^2/2})$ where $\mu = 0.0617$, $\kappa = 1.245$ and $\alpha = 0.0483$ [8]. Here, the parameters are calculated by fitting the equation to the known functionals (gradient expansion approximation (GEA) and revPBE), where the choice of the functional depends on the range of s . As a consequence, DFT calculations of intermolecular separation distances as well as the accuracy of vdW-DF interaction energies have been improved remarkably with vdW-DF-C09 functional.

The ground state energy and the density of a system is acquired by the simultaneous solution of the Kohn-Sham equations. The last three terms in the Kohn-Sham equations (Equation 2.30), which are also known as the effective potential, depend on the molecular orbitals and the density which we seek. Hence, the solution of Kohn-Sham equations requires a self-consistent approach.

Self-consistent field scheme (scf) is an iterative method to solve the Kohn-Sham equations and it creates a cycle of calculations. Starting point of an scf cycle is an initial guess for the density of the system. The Kohn-Sham operator and the effective potential is constructed with the initial guess of the density and Kohn-Sham equations are solved accordingly. The resulting density is compared to the initial guess in the first cycle and the estimated density is updated for the next cycle if they are not equal to each other. This procedure is repeated until an equivalency between the estimated density and the calculated density is observed.

2.2 Preliminary Calculations for Hexagonal Boron Nitride (h-BN)

The main purpose of this thesis is to examine the nanotribological properties of the h-BN within different configurations of systems involving several layers of h-BN, Au(111) and Au clusters.

Behavior of friction forces in an asymmetric interface, such as the one at hand here, depends sensitively on the relative magnitudes of the lattice constants. We shall elaborate on this topic in the following chapters. Due to this sensitive dependence, the numerical lattice constant to be used for the rest of this research must be calculated with sufficient accuracy. As a rule of thumb, systems that are going to be modeled

have to pass through a geometry optimization after they are constructed. The purpose of a geometry optimization is to find the geometry of the system with negligible strain where all forces on the atoms vanish, resulting in a minimized energy. Hence, after constructing the honeycomb structure of h-BN molecule with the given lattice vectors, geometry optimization has been performed. The molecular structure of h-BN is also shown in Figure 2.1. B is a group 3A metalloid, which has an electronic structure of $[\text{He}] 2s^2 2p^1$, whereas N is categorized as a reactive non-metal, whose electronic structure is $[\text{He}] 2s^2 2p^3$.

$$u_1 = a\left(\frac{3}{2}, \frac{\sqrt{3}}{2}, 0\right) \quad u_2 = a\left(\frac{3}{2}, -\frac{\sqrt{3}}{2}, 0\right)$$

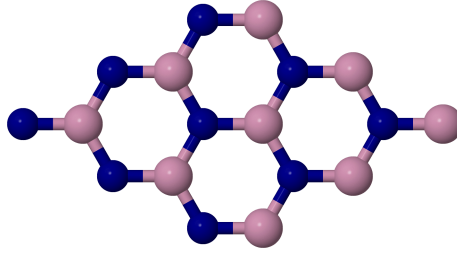


Figure 2.1: h-BN molecule

In our calculations, we have used Quantum Espresso software which is distributed free under the GNU public licence [14, 15]. We have chosen a large enough vacuum distance (near 15\AA) including the vdW interactions with the Cooper corrections [45] in our calculations. The kinetic energy cut-off for the wavefunctions is chosen to be 30 Ry and the kinetic energy cut-off for the charge density is chosen to be 300 Ry. This convention between the kinetic energy cut-off for wavefunction and for charge density is related to the usage of ultrasoft pseudopotentials. Sampling of the Brillouin zone is done according to Monkhorst-Pack scheme and taken as $10 \times 10 \times 1$ for the geometry optimization of BN. The cut-off values and k-points are chosen so that we have a feasible calculations for the problem at hand.

For the pursuit of finding the optimal lattice constant, several scf calculations around the experimental lattice constant value of h-BN has been performed and the result is shown in Figure 2.2. From this graph with a proper fit, a cell dimension of 2.74 Bohr radius (1.45\AA) that corresponds to the minimum value of the energy, E_{min} , has been

found. Lastly, a geometry optimization with the obtained lattice constant is performed to minimize the energy so as to ensure the system is stable.

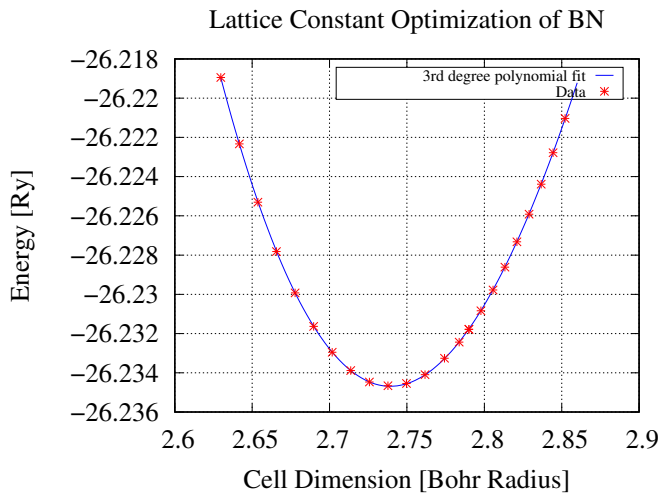


Figure 2.2: Energy vs Cell Dimension Graph of BN molecule

2.3 Preliminary Calculations for Bulk Gold (Au) and Au clusters

Au is a noble metal with the electronic structure of $[\text{Xe}] 4f^{14} 5d^{10} 6s^1$ and it almost never reacts to other materials although it is discovered in the last two decades that it can be used as a catalyst [7].

In order to model the bulk Au structure, the lattice constant of the crystal has been optimized to proceed further by using both primitive unit cell and conventional unit cell. Primitive unit cell of Au contains only one atom while the latter contains four atoms in its face-center cubic (fcc) lattice structure. The optimization has been performed for several number of k-points to find the convergence in the lattice parameter. Ideally, the resulting lattice parameters should be similar while the precision level of the numbers can change. To present the effect of k-point choice and the convergence of the lattice constant by increasing k-points, Figure 2.3 is shown. One can see that the lattice parameters for different k-points has similar values, converging to 4.11 Å.

Among the calculated k-points, $12 \times 12 \times 12$ has been chosen to proceed further calculations (Figure 2.4). Then, the corresponding lattice constant of Au, 7.76 Bohr

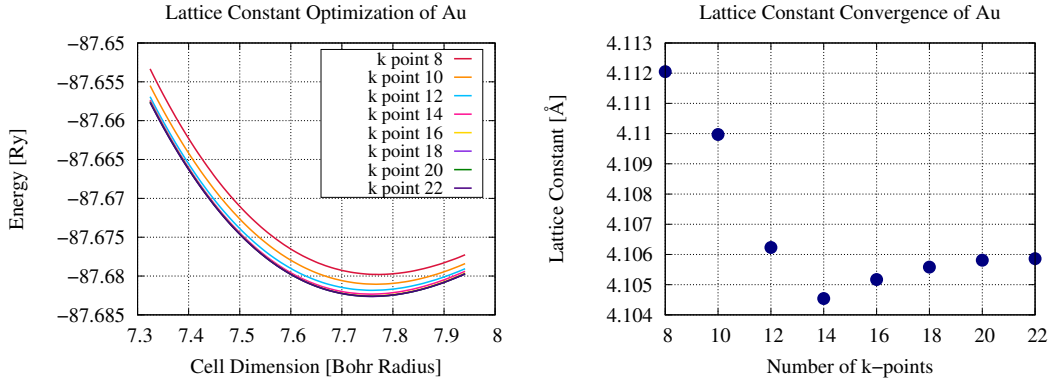


Figure 2.3: Effect of k-points on the lattice constant calculation of Au.

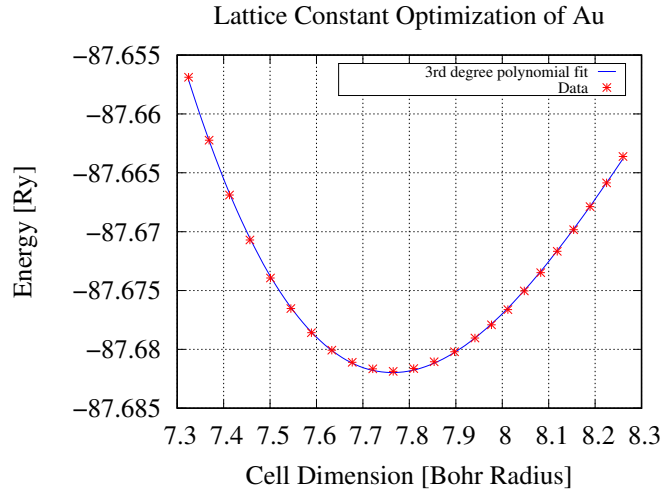


Figure 2.4: Lattice constant optimization of gold (Au) with 12 k-points in each direction

Radius, which corresponds to 4.11 Å, for this k-point mesh grid is found. This value has been used for the all Au included calculations in this thesis. The kinetic energy cut-off for the wavefunctions is chosen to be 30 Ry and the kinetic energy cut-off for the charge density is chosen to be 300 Ry. These parameters have been chosen so that we have fast enough computation time with a feasible calculation results.

After finding the lattice constant and deciding on the proper parameters, Au(111) surface of ABC stacking is constructed using the given unit vectors that create a plane which cuts the bulk Au of face centered cubic shape unit cell as shown in Figure 2.5.

Au(111) surface structure is chosen since it is the smoothest surface structure of Au among the other low index surfaces.

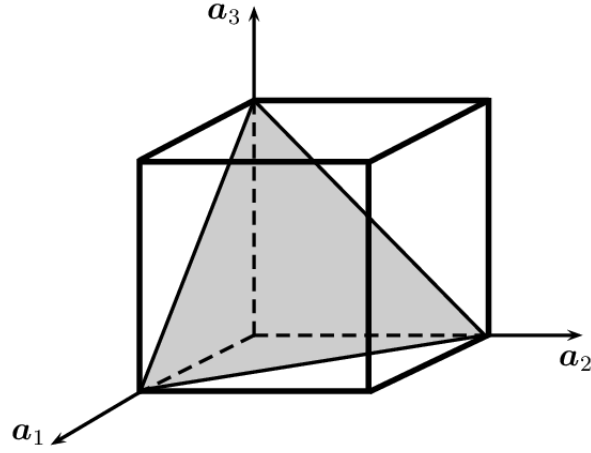


Figure 2.5: (111) surface representation. Adapted from [28].

$$u_1 = a\left(\frac{\sqrt{2}}{2}, 0, 0\right) \quad u_2 = a\left(\frac{1}{\sqrt{8}}, \frac{\sqrt{3}}{\sqrt{8}}, 0\right)$$

Once the first layer is constructed, second layer is obtained by displacing the first layer along the yz-plane using the vector $(0, -\frac{a}{\sqrt{6}}, \frac{a}{\sqrt{3}})$. Similarly, for the third layer, the first layer is shifted using the vector $(0, \frac{a}{\sqrt{6}}, \frac{2a}{\sqrt{3}})$. The distance between the layers in this structure is $\frac{a}{\sqrt{3}}$.

In order to obtain more sensitive results on the potential energy graph of the h-BN/Au(111) interface, the kinetic energy cut-off for wavefunction and the charge density has been increased to 60 Ry and 600 Ry, respectively, by compromising the computational time. Sampling of the brillouin zone is chosen to be $20 \times 12 \times 1$ for the h-BN/Au(111) interface with these updated cut-off values considering the asymmetric shape of the (2×2) h-BN and (3×1) Au(111) supercells.

Rhombic gold cluster is modeled by using two equilateral triangles side by side as they share a common edge. The initial bond length is chosen approximately 2.69 Å according to the study of Chinagandham et al. [40] and the geometry optimization is performed with the parameters of our simulation environment in order to find the correct structure with negligible strain. The real bond lengths in our system has turned

out to be fluctuating between 2.60 and 2.66 Å, making the structure a little distorted.

Similarly, the initial structure of the icosahedral and cuboctahedral gold clusters are modeled using the space vectors given in Table 2.1, followed by the geometry optimization of the clusters.

Table 2.1: Space vectors of icosahedron and cuboctahedron shaped gold clusters.

| cuboctahedron | icosahedron |
|---------------------------------|-------------------------------|
| $\frac{a}{\sqrt{2}}(0, 1, 1)$ | $\frac{a}{2}(0, 1, \theta)$ |
| $\frac{a}{\sqrt{2}}(0, -1, 1)$ | $\frac{a}{2}(0, -1, \theta)$ |
| $\frac{a}{\sqrt{2}}(0, 1, -1)$ | $\frac{a}{2}(0, 1, -\theta)$ |
| $\frac{a}{\sqrt{2}}(0, -1, -1)$ | $\frac{a}{2}(0, -1, -\theta)$ |
| $\frac{a}{\sqrt{2}}(1, 1, 0)$ | $\frac{a}{2}(1, \theta, 0)$ |
| $\frac{a}{\sqrt{2}}(-1, 1, 0)$ | $\frac{a}{2}(-1, \theta, 0)$ |
| $\frac{a}{\sqrt{2}}(1, -1, 0)$ | $\frac{a}{2}(1, -\theta, 0)$ |
| $\frac{a}{\sqrt{2}}(-1, -1, 0)$ | $\frac{a}{2}(-1, -\theta, 0)$ |
| $\frac{a}{\sqrt{2}}(1, 0, 1)$ | $\frac{a}{2}(\theta, 0, 1)$ |
| $\frac{a}{\sqrt{2}}(1, 0, -1)$ | $\frac{a}{2}(\theta, 0, -1)$ |
| $\frac{a}{\sqrt{2}}(-1, 0, 1)$ | $\frac{a}{2}(-\theta, 0, 1)$ |
| $\frac{a}{\sqrt{2}}(-1, 0, -1)$ | $\frac{a}{2}(-\theta, 0, -1)$ |
| $\frac{a}{\sqrt{2}}(0, 0, 0)$ | $\frac{a}{2}(0, 0, 0)$ |

where a is the bond length and $\theta = \frac{1+\sqrt{5}}{2}$ is the golden ratio in Table 2.1 [35].

The further discussion about the systems and the calculations performed so far are provided in the next chapters along with the nanotribological behavior of these interfaces constructed.

CHAPTER 3

NANOTRIBOLOGICAL PROPERTIES OF THE TWO DIMENSIONAL HEXAGONAL BORON NITRIDE

3.1 Friction Between Two h-BN Layers

Hexagonal Boron Nitride (h-BN) is a wide-band gap semiconductor while its band gap slightly varies depending on the stacking; namely AA, AB, AD, AE and AF [51]. Hexagonal boron nitride has the honeycomb lattice structure as in the case of graphite and it has the similar lubrication performance with graphite. These similarities between them makes h-BN to be called “white graphite” [4].

Materials based on boron nitride have been used as electrical insulators and thermal conductors for the last decades due to its high conductivity property. It also exhibits outstanding luminescence performance which makes it an effective candidate for ultraviolet region light emitting devices [38] such as ultraviolet laser devices which are increasing in demand because they have crucial applications to the sterilization, optical storage and nanosurgery [47].

In-plane bonding of h-BN is barely affected by the uniaxial pressure thanks to the strong in-plane covalent bonds which are much more stronger than the inter-plane weak van der Waals bonding [21].

We start our calculations by constructing the h-BN structure as it has been discussed in the preliminary calculations in chapter 2 and lattice constant of h-BN is found to be 1.45 Å with the DFT parameters we have used. A system consists of two BN layers has been modeled and one BN layer is placed over another to find the tribological

behavior of the interface. Due to the symmetrical nature of the model, whether the top layer or the bottom layer is mobile does not have an effect on the calculation results. Therefore, we have kept the bottom layer fixed during the calculations while we pull the the upper layer along x-direction (armchair) towards the asperities of the fixed BN layer. The atoms of the fixed BN layer provide a periodic potential for the upper mobile BN layer owing to the periodicity of the material. During the sliding, we have also changed the vertical distances between the materials from 2.9 Å to 3.5 Å by increasing the separation in steps of 0.17 Å. Then, we calculated the adhesion energy along the sliding path at each vertical distance. Adhesion energy between the two BN sheets and the friction force during the sliding are indicated in Figure 3.1.

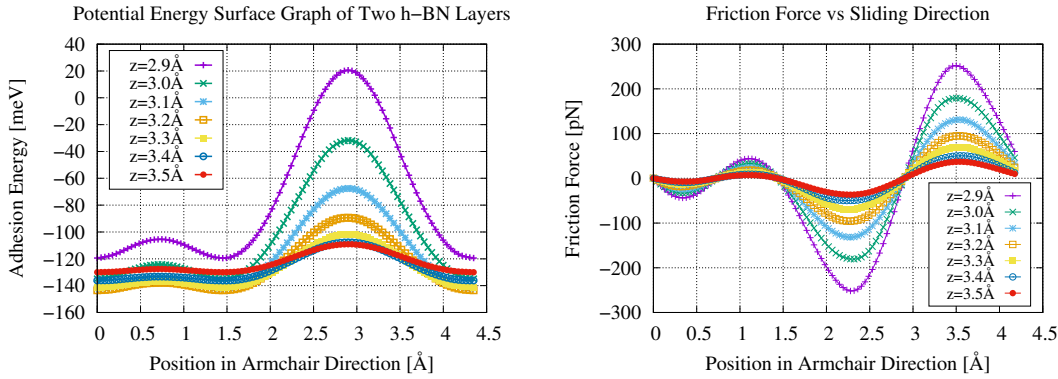


Figure 3.1: Adhesion energy and friction force at the h-BN/h-BN interface in armchair (x) direction

We have further examined the interface by taking the three vertical distances out of seven (from 2.9 Å to 3.5 Å) and considered the interface at 2.9 Å, 3.0 Å and 3.2 Å. Then, we have carried out our investigation by observing the directional dependence of the friction force. Thus, we have pulled the upper h-BN layer over the bottom one along armchair (x) and zigzag (y) directions as the directions are shown in Figure 3.2. The starting point of the two h-BN layers are the same for each sliding direction.

In Figure 3.4, the graph at the left shows the adhesion energy at the interface along the armchair (x) direction. The hills and the dips of the graph correspond to the different locations of two BN layers with respect to each other. Reguzzoni et al. [41] indicated in their study with two graphene layers that the first maximum (smaller peak) cor-

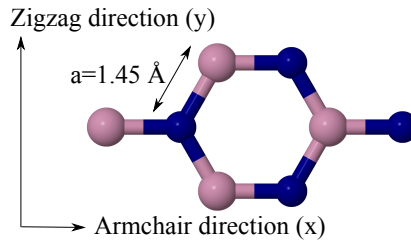


Figure 3.2: Honeycomb structure of BN

responds to the potential energy surface (PES) saddle point and the highest (global) maximum is the AA stacking. Since graphene and BN molecule have similar molecular structure, it is safe to say the smaller peak in the adhesion energy in Figure 3.4 is called PES saddle point as in the case of Reguzzoni's study and global maximum is the AA stacking where the same atoms of the two layers are completely aligned. The positions of the two materials at the minimum, maximum and the saddle points are shown in Figure 3.3.

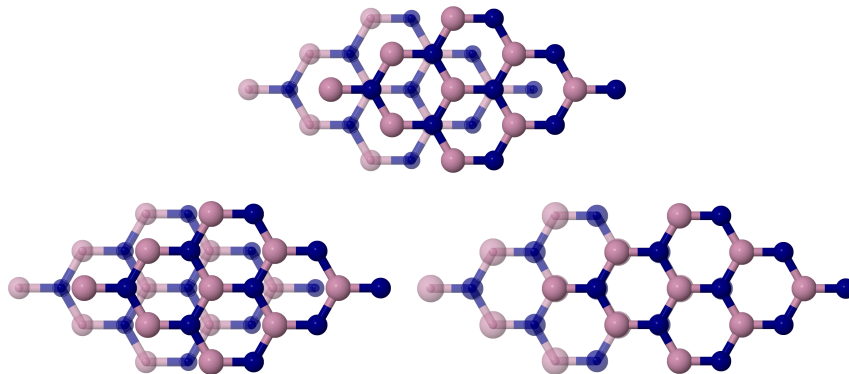


Figure 3.3: Above: Minimum point configuration of the two h-BN layers and the starting point of the motion. Left: two layers of BN at saddle point. Right: two layers of BN at AA stacking while sliding in armchair (x) direction. The atoms of the bottom h-BN layer are shown in relatively small sizes and pale colors compared to the atoms of the upper layer which are larger and have brighter colors.

Adhesion energy between the two sheets of h-BN is calculated using the following equation.

$$E_{adh} = E_{bilayer} - 2 \times E_{layer} \quad (3.1)$$

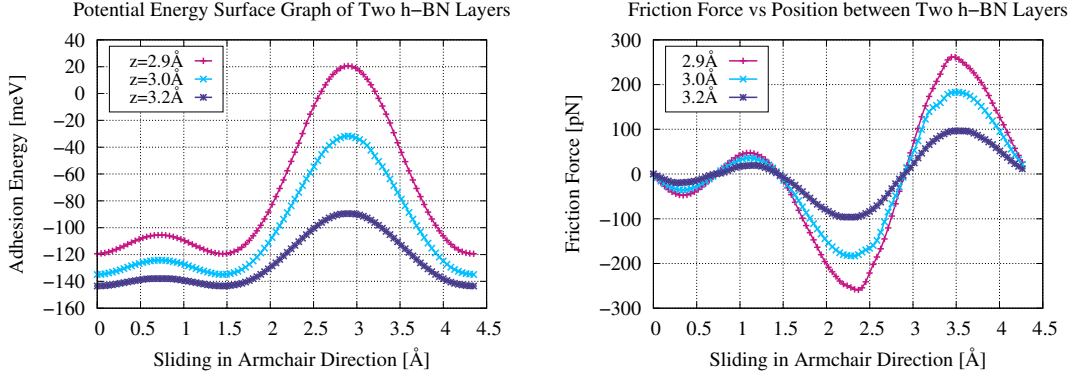


Figure 3.4: Adhesion energy and friction force of the h-BN/h-BN along armchair (x) direction

Although the lateral friction force which is displayed in Figure 3.4 for three different separations appears to be counter-intuitive from a macroscopic point of view, it is correlated to the fact that the corrugation, defined as the energy difference between the minimum and the maximum of the energy landscape, decreases with increasing separation for the separations studied here.

To understand the friction behavior at zero load, we repeat the above calculation by means of conduction geometry optimization at every point along the sliding path. During these calculations, we only allow the BN layer to relax along the z axis while keeping x and y coordinates fixed. This allows us to map the adhesion energy at zero load as a function of x, which we present in Figure 3.5.

From the adhesion energy calculated at different heights, the lateral friction force can be calculated using

$$F_{fric} = -\frac{\partial E_{adh}}{\partial x} \quad (3.2)$$

In the calculation of the derivative, we use a centered-difference approach to minimize

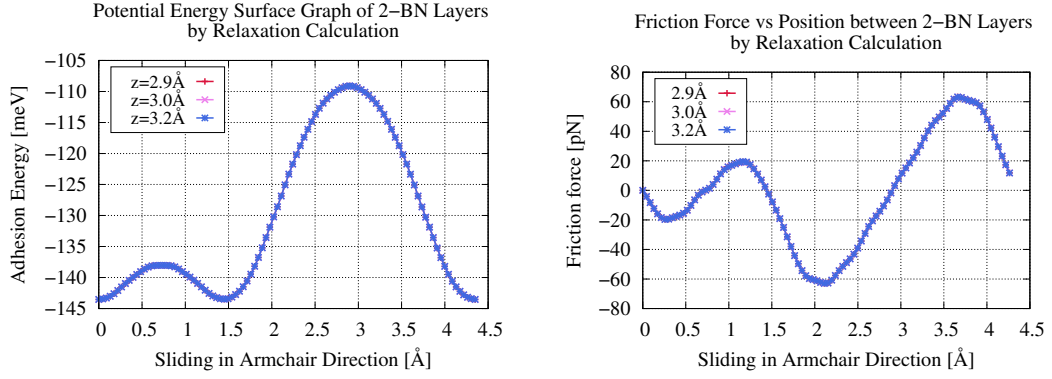


Figure 3.5: Adhesion energy and friction force between the two h-BN along x -direction using the geometry optimization method at every point during the sliding.

the error :

$$F_{fric}(x) = - \lim_{x \rightarrow 0} \frac{E_{adh}(x + \varepsilon) - E_{adh}(x - \varepsilon)}{2\varepsilon} \quad (3.3)$$

The lateral friction forces calculated for the geometry-optimized case shown in Figure 3.5 presents three different initial separations, which all converge to the same result. This is evidence that our convergence criteria for the geometry optimization is tight enough. As expected, the zero-load friction forces are much smaller compared to the fixed-separation results since these separations correspond to larger loads.

Next, we present friction forces along the zigzag (y) direction. Directional dependence of the friction is worth to examine since sliding directions affect the stacking of the two materials leading to a different topology of the potential energy surface. The results for sliding along the zigzag direction is shown in Figure 3.7.

In all of the calculations presented, the positive side of the friction force graphs are not of interest since they correspond to the “downhill” motion of the atoms. The system is at either saddle point or at global maximum point which are not the most stable configurations for the system. Small disturbances can cause a motion on the system and the atoms of the upper layer fall to the nearest minimum point by themselves. Thus, we take into account only the negative parts of the friction force for the average friction force calculations.

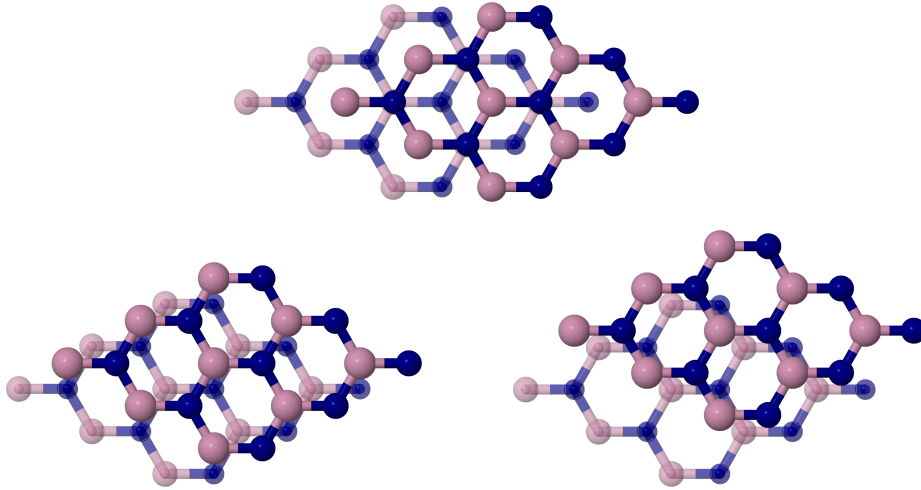


Figure 3.6: Two h-BN layers, upper layer is pulled through zigzag (y) direction. Above: The starting point of the sliding.

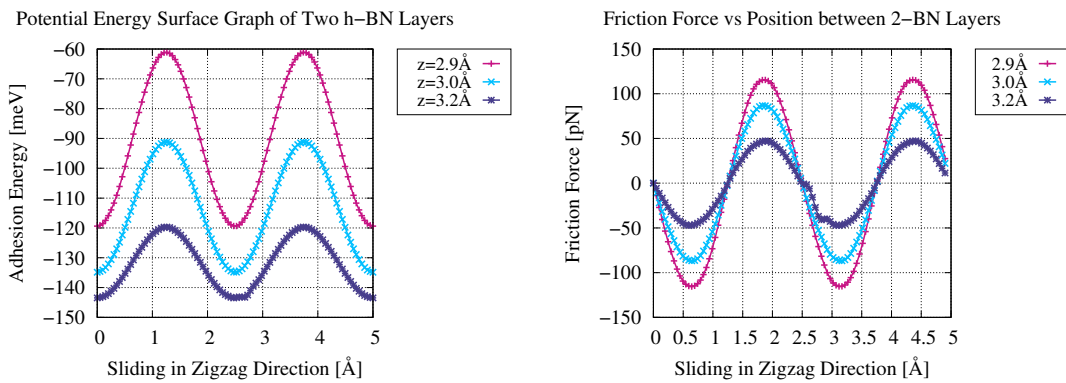


Figure 3.7: Adhesion energy and friction force of the h-BN/h-BN along zigzag (y) direction

3.1.1 Discussion

To facilitate the comparison of lateral friction forces in different directions, we collect all our friction force results in a single plot at the constant vertical distance of 3.0 in Figure 3.8.

Although the overall features of the profiles are similar, the maximum value of friction force for zigzag sliding is less than that of the armchair sliding since there is no repeated ontop-ontop coincidence among the same atoms. The Boron atoms on

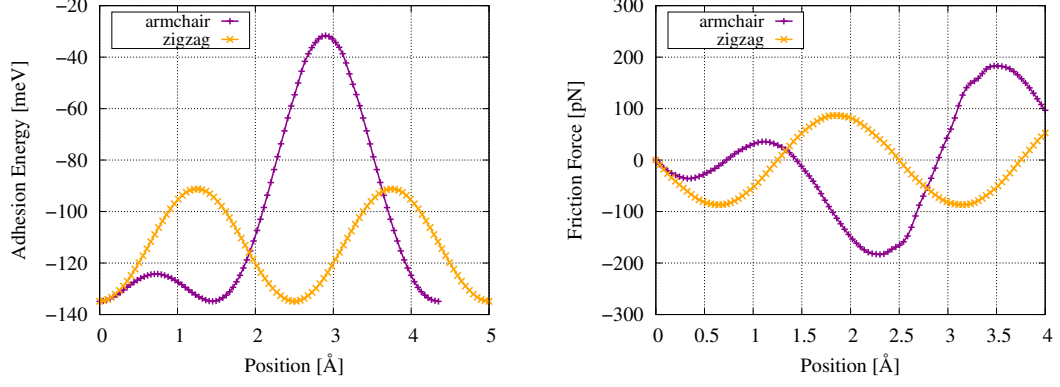


Figure 3.8: Comparison of the h-BN/h-BN results

the upper layer coincide with the N atoms of the lower layer recurrently during the zigzag sliding. On the other hand, there is an repeated ontop-ontop coincidence along with the B-N coincidence during the armchair sliding. Hence, the saddle point is, of course, absent in the case of the zigzag configuration. All the maxima correspond to a global maximum and the magnitude is much smaller than that of the armchair results. Since these two directions represent the highest possible symmetry, we expect the friction forces obtained in these directions to be upper limits for the entire interface with the initial stacking at hand.

Next, we focus on the average friction forces, which would correspond to forces felt by a realistic experiment. The average friction force calculation has been performed for different sliding direction and shown in Table 3.1.

Average friction force has been calculated using following deduction.

$$F_{fric}^{average} = \frac{\Delta x}{L_{total}} \sum_i F_{fric}(i) \quad (3.4)$$

where Δx is the infinitesimal sliding distance, L_{total} is the projection distance of the negative parts of the friction force curve to the lateral axis and $F_{fric}(i)$ is the friction force at the i^{th} position.

Table 3.1: Average Friction Force between h-BN/h-BN for Different Sliding Directions

| Average Values of Friction Force per unit cell [pN] | | |
|---|--------------------|------------------|
| Separation distance [Å] | Armchair direction | Zigzag direction |
| $z=2.9$ | 122.46 | 84.00 |
| $z=3.0$ | 90.50 | 62.80 |
| $z=3.2$ | 47.45 | 34.19 |

3.2 Friction Calculation Between Two h-BN Layers Under Applied Normal Force

Materials properties at nano-scale tend to differ under an applied load, therefore, require further analysis. Nanotribology research with AFM/FFM experiments reveal the load dependency of the friction force at a given interface and computer simulations of materials under load may provide a benchmark to the future experiments. In this section, we report the nanotribological behavior of the h-BN/h-BN interface under applied normal force.

In a system, any vertical position between two materials which is different than the equilibrium distance results in a vertical strain at the interface. This vertical strain is the load force and it depends on the distance between the tip and the surface. We start finding the load force as a function vertical distance at the h-BN/h-BN interface. Load force is found by taking the negative derivative of the total energy with respect to the vertical distance between the two sheets of h-BN.

$$F_{load} = -\frac{\partial E_{total}}{\partial z} \quad (3.5)$$

At every lateral position during sliding, there exists a corresponding equivalent vertical distance where the system is at the minimum energy configuration i.e at zero load. For the pursuit of reaching the friction force under load, graphs of total energy vs separation between two h-BN sheets are drawn for each lateral position during the sliding along armchair (x) direction. At each step of the sliding process, upper layer

of the h-BN is moved by 0.17 \AA from the initial point of 0 \AA to the 4.35 \AA , totaling to 25 steps. For simplicity, we have left out some intermediate steps of the results and shown the rest of them at the three graphs corresponding to different lateral (x) positions as seen in Figure 3.9.

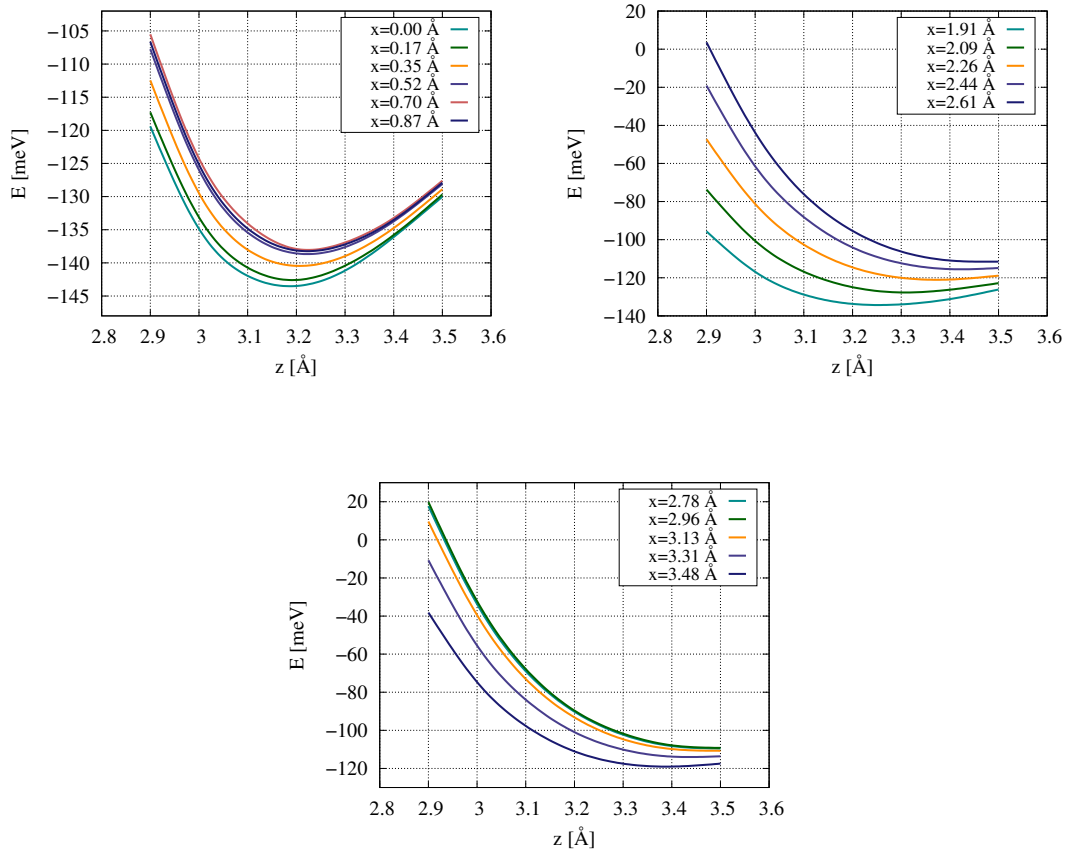


Figure 3.9: Total Energy vs vertical distance at different lateral (x) positions at the interface of the h-BN/h-BN

The vertical distance corresponding to the minimum energy value for each lateral position can be found from Figure 3.9. Any other vertical position at which two h-BN layers are located, distinct from the equivalent vertical distance will provoke a normal (load) force. Therefore, the negative derivative of Figure 3.9 with respect to the vertical distance (z) gives Figure 3.10.

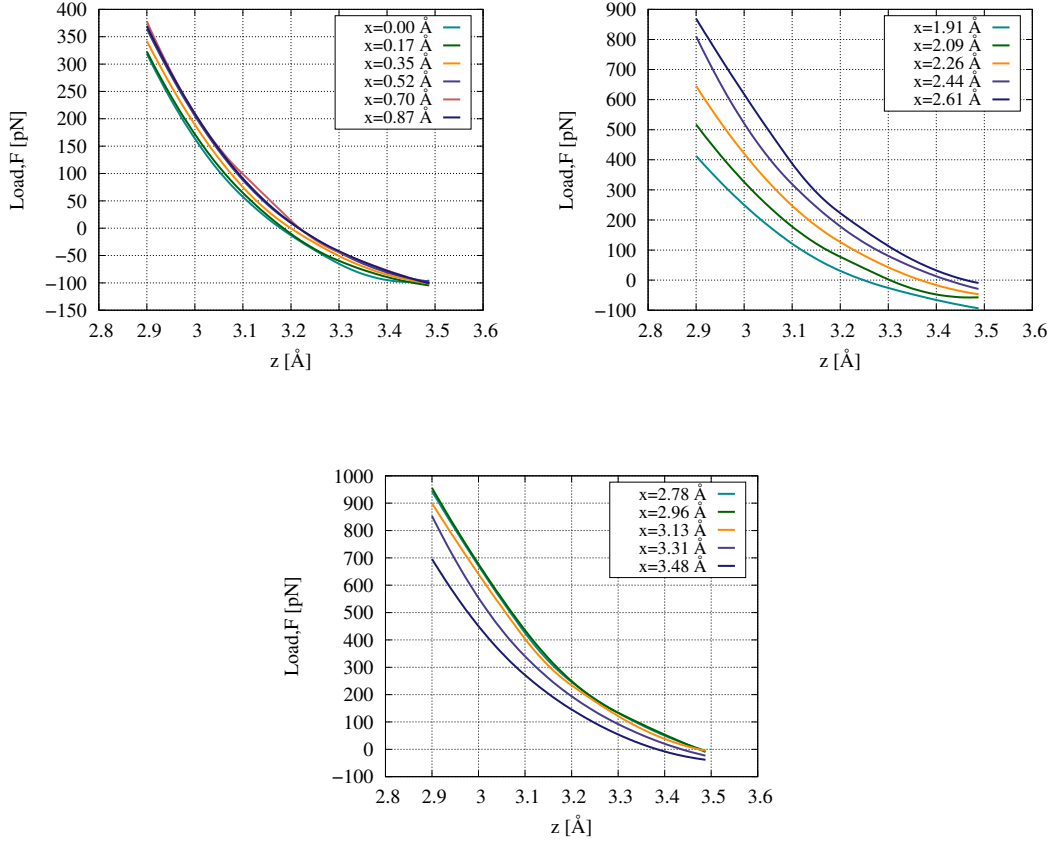


Figure 3.10: Load force vs vertical distance at different lateral positions (x) at the interface of h-BN/h-BN

3.3 Contact Area Decision for Load Force Calculations

Load force calculations at the interface of the h-BN/h-BN has performed by starting with the decision of an experimentally feasible contact area since DFT calculations so far have been achieved over one unit cell and we seek for our results to be comparable with experimental research.

For this purpose, contact area estimation has to be done. For microscopic friction, this is not straightforward since the real contact area is different than the apparent one. However, relation between area and load force can be implemented from continuum mechanics models which assume a sphere tip in contact with a flat plane that is the sample. Yet, the models still do not represent the exact result since load-area relation does not purely depend on geometry but the strength of the adhesive forces

as well [11]. Therefore, it is not possible to find real contact area but it is possible to make a close approximations by using the continuum mechanics models since the models are generally fit to the experimental data.

In the Leung and Goh's study, the contact area is said to be $10^{-15} m^2$ which corresponds to $10,000 nm^2$ AFM tip of Si_3N_4 with pyramidal shape tip indicated by the manufacturer [29]. In the paper, it has been said that they used $0.1 \mu N$ load force to enhance the tip-surface interaction.

In another study conducted by Bhushan and Kulkarni, Si_3N_4 and diamond tip has been used over various samples such as SiO_2 and $Si(111)$. The radii of the tips that are used in the study are $R = 100 nm$ for NTT/FFM instrument with applied forces being in the range from 1 to $50 \mu N$ and $R = 150 nm$ for the AFM/FFM instrument with the applied normal force being in the range from 50 to $150 nN$ [6]. In the light of these information and assuming the contact area being circular region, the estimated contact area corresponds to the given radii can be calculated as $30,000 nm^2$ and $67,500 nm^2$ respectively using the area formula for circle which is πR^2 . Figure 3.11 is added on to show some of the results of Bhushan and Kulkarni's work.

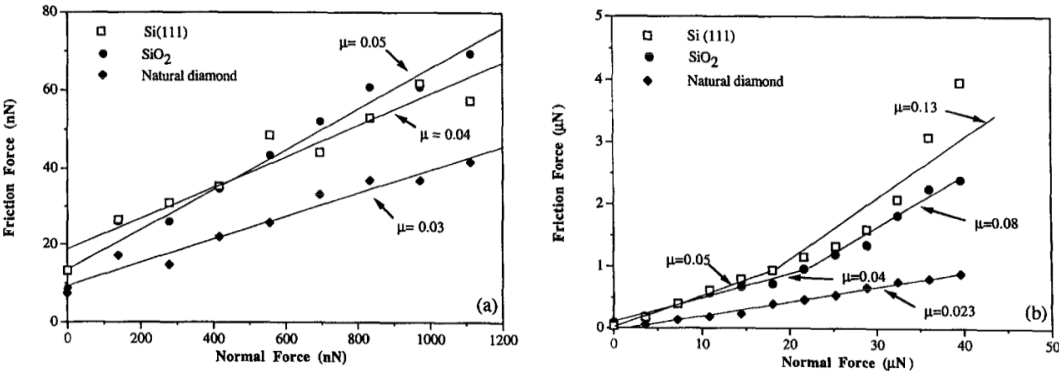


Figure 3.11: Friction force as a function of normal force for virgin $Si(111)$, SiO_2 coating and polished natural diamond. Measurements were made on a fresh $1 \mu m \times 1 \mu m$ scan areas using a diamond tip with a maximum force to (a) about $1300 nN$ and (b) $40 \mu N$ as cited from Leung and Goh's study [6]

There are other studies examining the effects of the load force on the contact area in nanoscale systems. A comprehensive study has been done by Enachescu et al.

using diamond(111)/tungsten carbide single asperity contact with UHV-AFM having the tip radius of $R = 110 \text{ nm}$, contact area of which turns out to be approximately $35,000 \text{ nm}^2$. In their work, in order to be able to describe the tip-sample interaction they also showed some continuum mechanics models that fit to the experimental data quite convincingly such as Derjaguin-Müller-Toporov Model (DMT Model). According to DMT model studied by Enachescu et al., load force and contact area is related to following equation:

$$A = \pi \frac{R^{2/3}}{K^{2/3}} (L + 2\pi\gamma R)^{2/3}$$

where R is the tip radius, γ is the necessary work per unit area in order to separate tip and sample in contact to infinity. K is defined as $K = \frac{4}{3} \times E^*$ with E^* is the combined elastic modulus giving by the equation $E^* = [(1 - \nu_1^2)/E_1 + (1 - \nu_2^2)/E_2]^{-1}$. Here E_1 and E_2 are the Young's moduli and ν_1 and ν_2 are the Poisson's ratios of the sphere and plane respectively [11]. They also examined the contact area dependence of friction force in Figure 3.12.

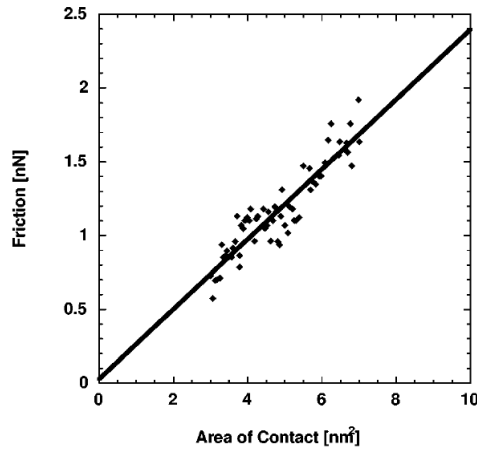


Figure 3.12: Change in friction force by contact area studied by Enachescu et al. [11]

From the literature research, it has been understood that the contact area between the tip and the sample is roughly taken in the range between $10,000$ and $70,000 \text{ nm}^2$ in several studies. Thus, it may be convenient to choose contact area to be $20,000 \text{ nm}^2$ in our study.

Since the contact area has been decided from the literature research, the graphs shown

in the Figure 3.10 is updated with the chosen contact area to proceed further. New results are illustrated in Figure 3.13. As seen, for a $20,000 \text{ nm}^2$ contact area, load force is in the μN range. When thought of the distances between two h-BN layers altered from 2.9 \AA to 3.5 \AA , this μN range may be expected. Yet, one should keep in mind that this conversion is only assumptive since conversion process cannot be exact as it has been explained in detail above. This is done in order to provide a comparison for the future experimental research that will use these materials.

After deciding the contact area and recalculating the results, we have chosen the magnitude of the load force that we wish to apply to the interface. For starters, $100 \mu\text{N}$ load force is chosen to analyze the interface.

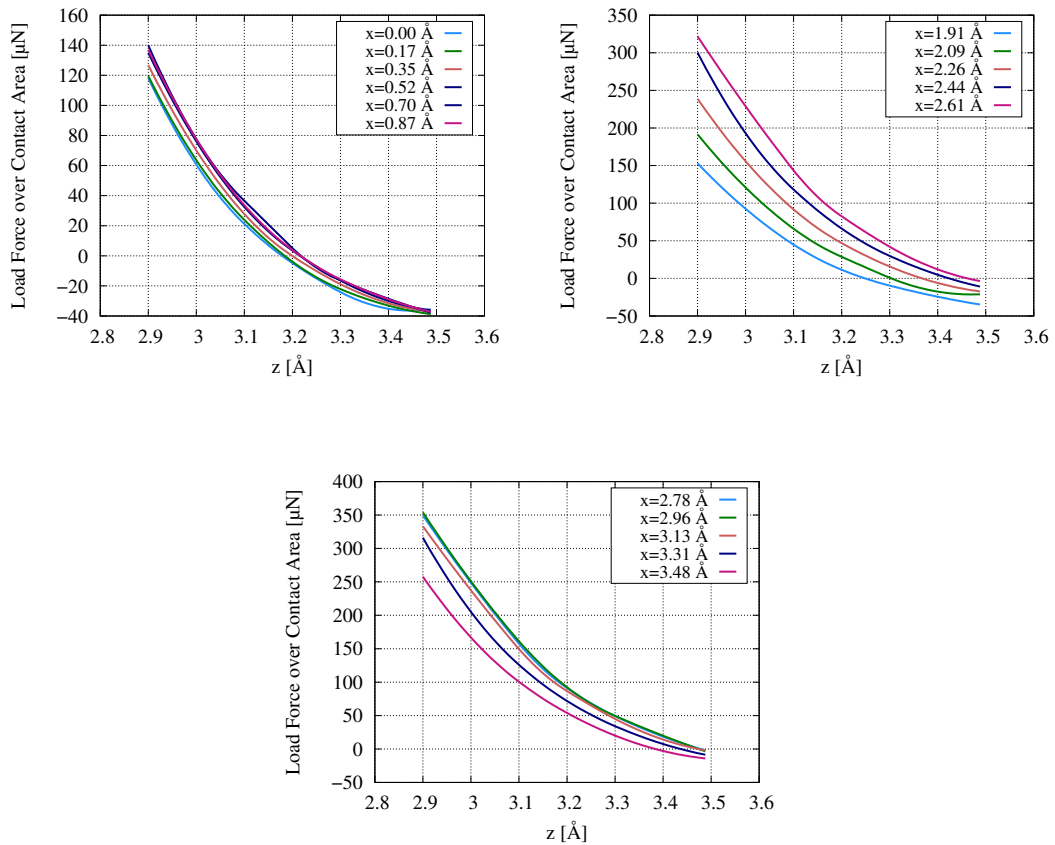


Figure 3.13: Load Force vs vertical distance (z) over the contact area of $20,000 \text{ nm}^2$

Corresponding equivalent vertical distances at each lateral position are found from Figure 3.13 under the chosen magnitude of the load using spline interpolation. At this point, energy values corresponding to these z -distances are computed from Figure 3.9

again with the help of the spline interpolation. Then, Figure 3.14 shows how adhesion energy and the friction force at the interface during the sliding changes at each lateral position under $100 \mu\text{N}$ load. The friction force is found with the same differentiation method as before.

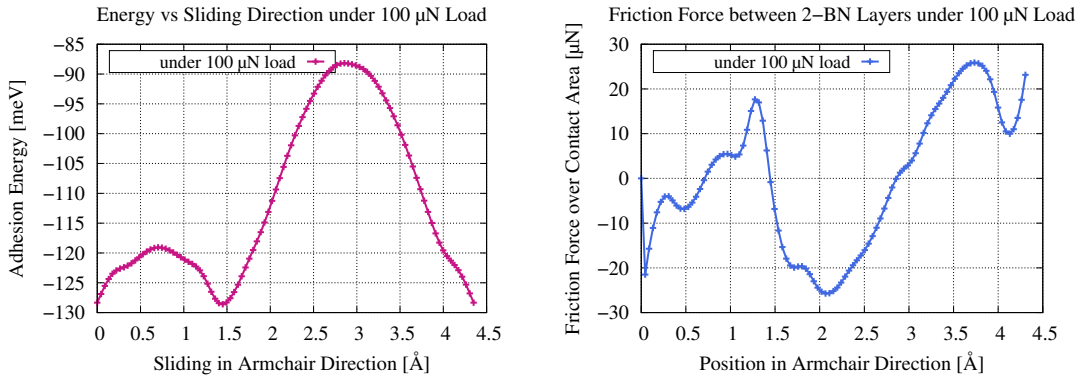


Figure 3.14: Adhesion energy and friction force at the h-BN/h-BN interface under $100 \mu\text{N}$ load

The method to find the friction force over a contact area is multiplying the results which is found for one unit cell by the chosen contact area and then dividing it into the area of the one unit cell at hand. In this case, the area of the primitive unit cell of h-BN is 0.054 nm^2 .

In order to be able to make a more precise inference from Figure 3.14, the resolution of the calculation is increased and the results are plotted again. The sliding path is divided into 75 steps instead of 25 steps as done for the $100 \mu\text{N}$ case above. By this way, DFT calculations have been performed for closer consecutive steps of positions, leading to an increased resolution in the calculations. The results can be seen in Figure 3.15. As seen, when the resolution is increased, there appear few more points that the friction force make peaks. We remind the reader that the contact area information is implemented only on the friction calculations. Graph of adhesion energy is still over one unit cell since there is no need for contact area information of energies to calculate friction. Friction force is related to the curvature of the adhesion energy graph, not to the magnitude. Our aim is to see the load dependency of the average friction force, therefore, several more calculations have been performed using $50 \mu\text{N}$,

60 μN , 70 μN , 80 μN , 90 μN load forces over the chosen contact area other than 100 μN . The results are shown in the Figure 3.16.

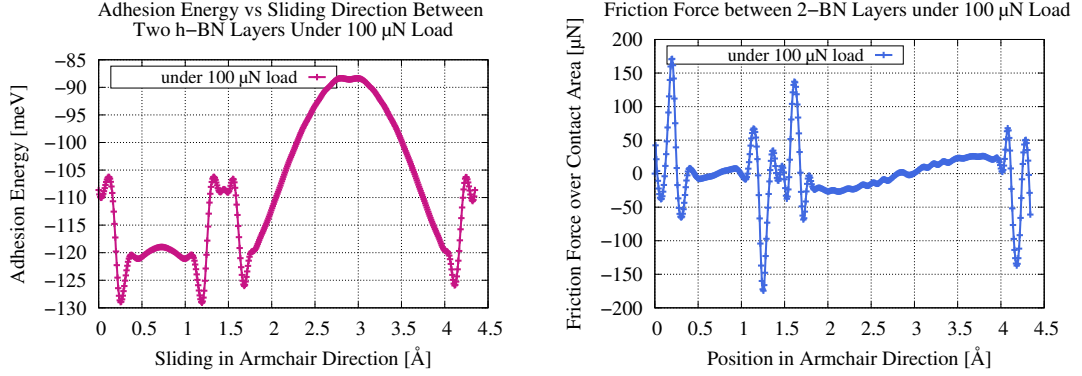


Figure 3.15: Adhesion energy and friction force at the h-BN/h-BN interface under 100 μN load with increased calculation steps

In order to see how the electronic orbitals are arranged, average charge density difference calculations have been performed at the lateral positions of 1.0 \AA and 3.0 \AA . Corresponding configurations at those lateral positions are shown in Figure 3.17 and the average charge density difference results under 50 μN and 90 μN loads are shown in Figure 3.18. At first glance, one can realise the magnitude of the average charge density is a little higher for the 90 μN case as compared to the 50 μN case. It can be also seen that the results of the lateral positions $x = 1 \text{\AA}$ and $x = 3 \text{\AA}$ coincide except that there is two extra peaks in the $x = 1 \text{\AA}$ case under 50 μN load. The negatively charged peak at $x = 1 \text{\AA}$ becomes positively charged when the magnitude of the load is increased to 90 μN . Similarly, almost neutral fluctuating part at the interface under 50 μN gets positively charged for the 90 μN case as well. We observe that the distribution of the average charge at the interface for different lateral positions are different than each other.

We have calculated the average friction force and the friction coefficient at this interface and reported the results in Figure 3.19 and Table 3.2. We observed that the average friction force increases whereas the friction coefficient decreases when the load is increased. The friction coefficient is calculated by using Equation 3.6.

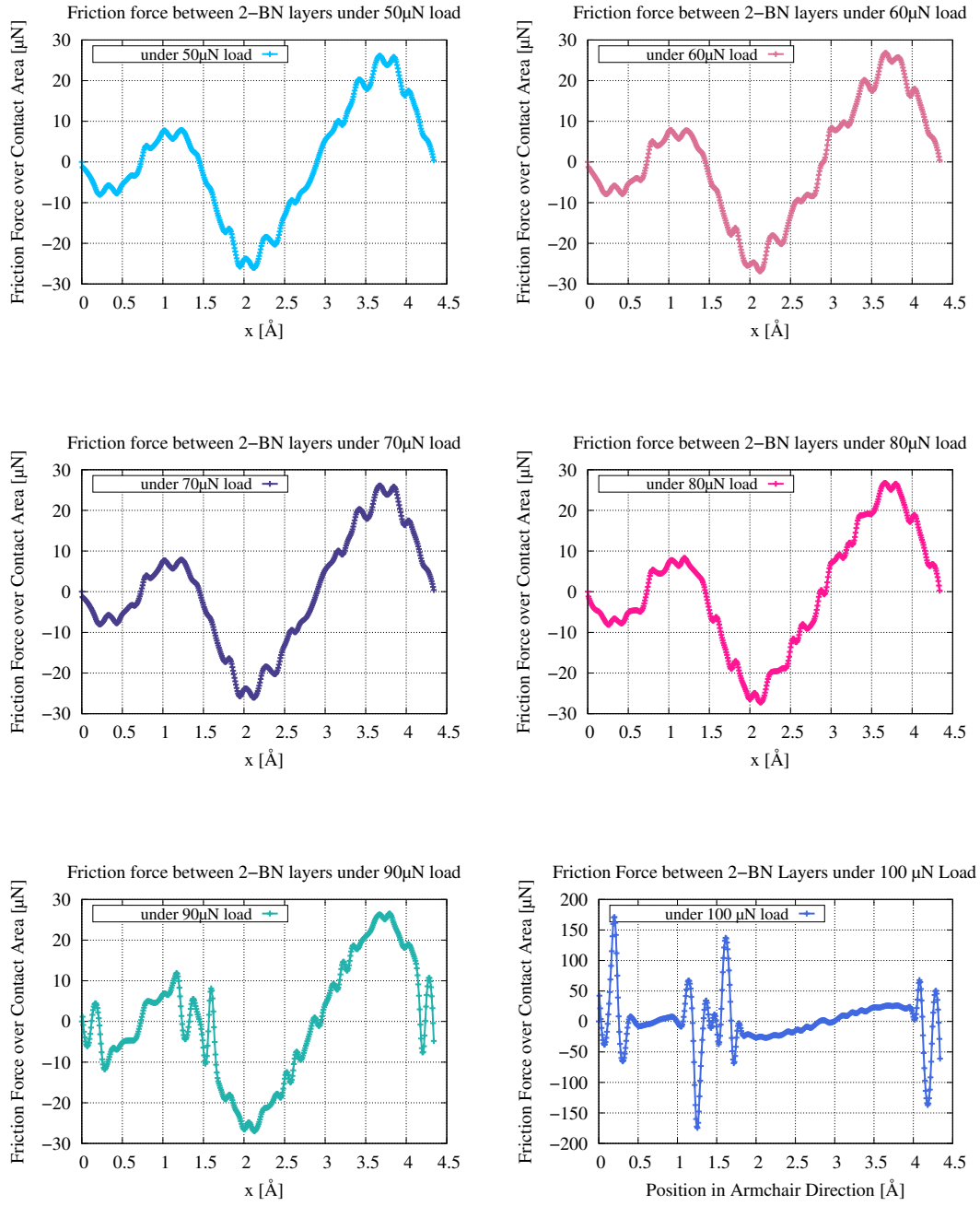


Figure 3.16: Friction force between two BN sheets under several load forces

$$F_{average} = \mu N \quad (3.6)$$

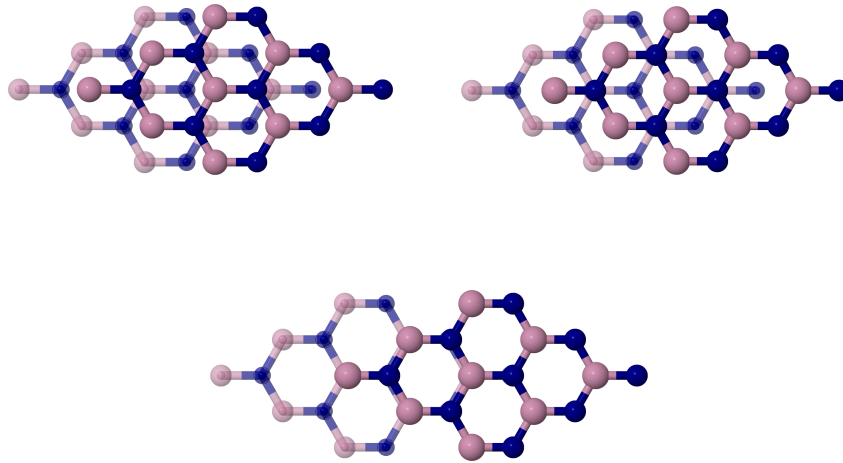


Figure 3.17: Top left: Upper BN is located at 1.0 Å with respect to the initial configuration of AB-stacking. Top right: at 1.5 Å. Bottom: at 3.0 Å.

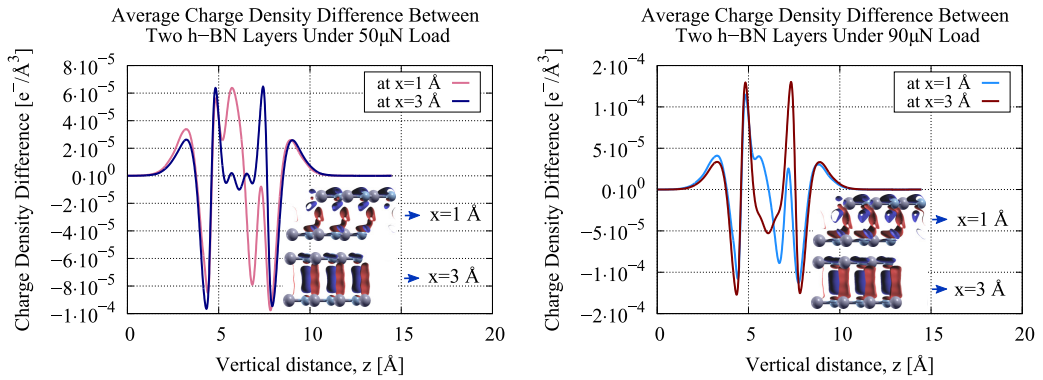


Figure 3.18: Average charge density difference at the h-BN/h-BN interface

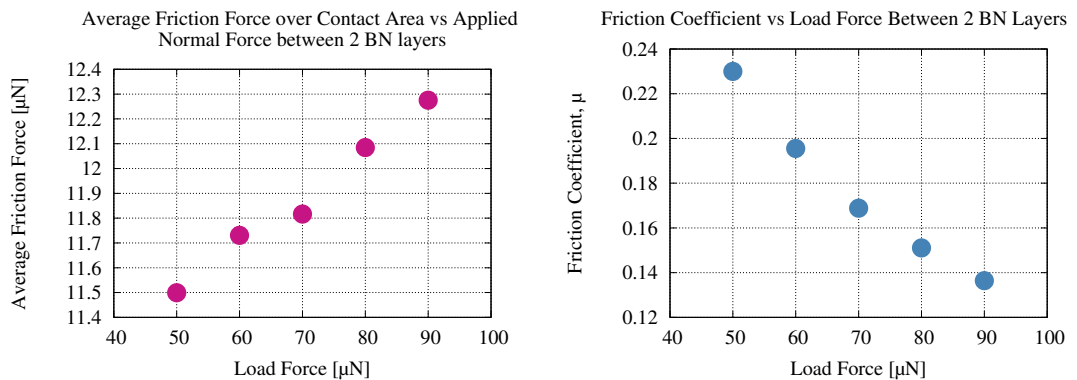


Figure 3.19: Change in average friction force over the contact area and the friction coefficient change by the load.

Table 3.2: Friction coefficient and average friction force over the contact area at the h-BN/h-BN interface under applied load

| Friction Coefficient, μ and F_{average} under Applied Loads, N | | |
|---|--|-----------------------|
| Applied Load [μN] | Average Friction Force [μN] | Friction Coefficients |
| 50 | 11.50 | 0.23 |
| 60 | 11.73 | 0.20 |
| 70 | 11.82 | 0.17 |
| 80 | 12.08 | 0.15 |
| 90 | 12.28 | 0.14 |
| 100 | 28.45 | 0.28 |

3.4 Friction Calculation Between 3, 4 and 5 h-BN Layers

It is well-known that the lamellar structures of the two-dimensional materials vary in behavior compared to their single layered structures. We have improved our h-BN/h-BN interface by adding a third layer to the system and moved one layer over others. ABA stacking of three infinite h-BN sheets have been prepared and the top layer which lies on the A stacking configuration has been pulled to the armchair (x) direction. In order to find where to place the second layer over the bottom layer, a geometry optimization has been done and equilibrium distance of 3.18 Å has been found. Next, the third layer was placed at desired distances which in this case varies between 2.9 to 3.5 Å. After the calculations at each sliding distance, adhesion energy and the friction force at the interface has been obtained and shown in Figure 3.21.

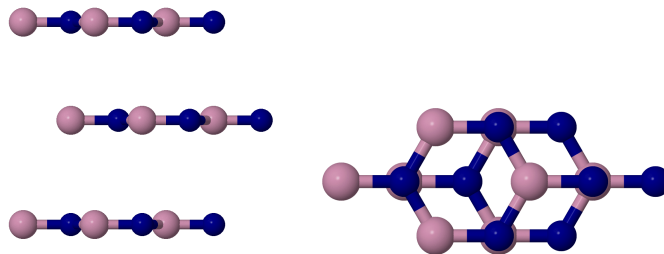


Figure 3.20: Three layered h-BN

We have followed the similar analysis as before and calculated the change in the

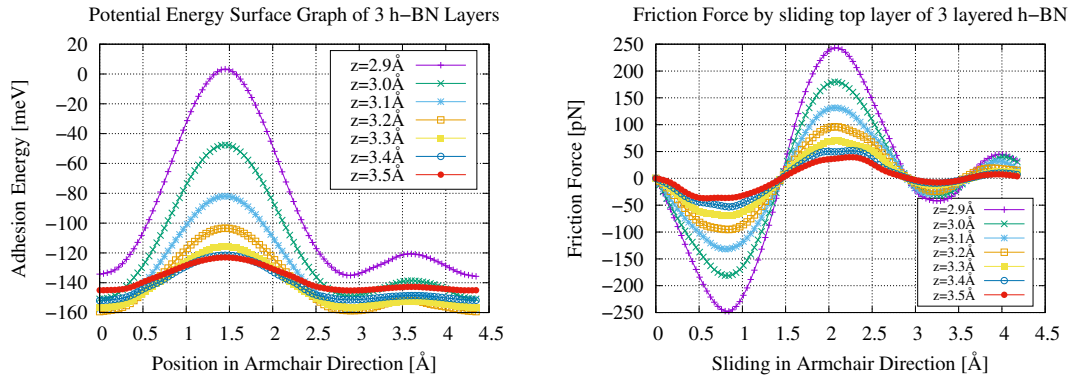


Figure 3.21: Adhesion energy and friction force at the interface of 3 layered h-BN/h-BN along x-direction

average friction force by the distance between second and the third layer. It is shown in Figure 3.22.

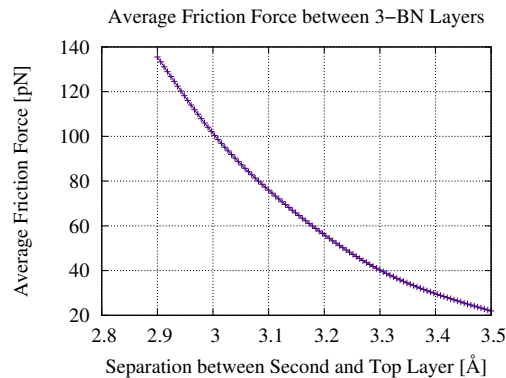


Figure 3.22: Average friction force at the interface of 3 layered h-BN/h-BN

After placing the second h-BN layer, third one has been placed at the equilibrium distance of 2.99 Å which is found by the same way as before with the geometry optimization. Then, the fourth layer has been placed between the distances of 2.9 to 3.5 Å. The results are shown in Figure 3.24.

Change in the average friction force with respect to the distance between the third and the fourth layer has been calculated and shown in Figure 3.25.

Similarly now, fourth layer has been placed over the previous system at the equilib-

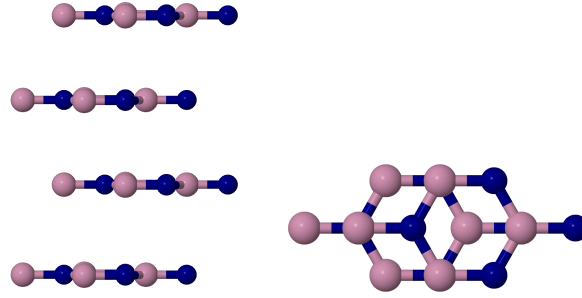


Figure 3.23: Four layered h-BN

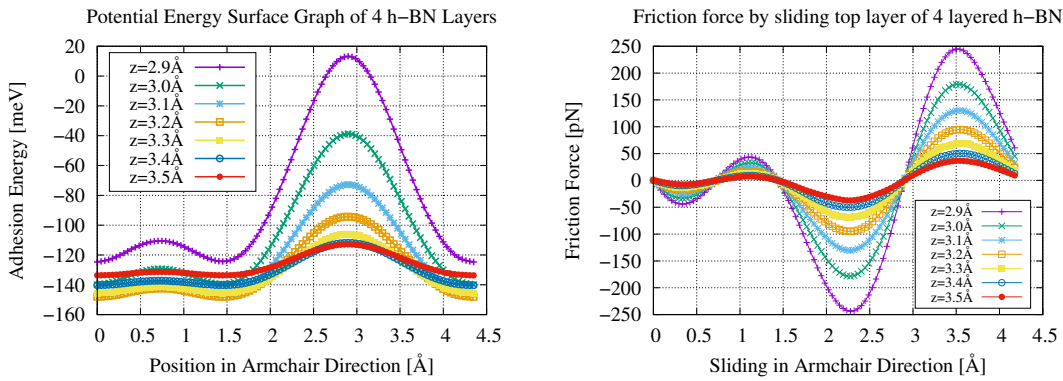


Figure 3.24: Adhesion energy and friction force at the interface of 4 layered h-BN/h-BN along x-direction

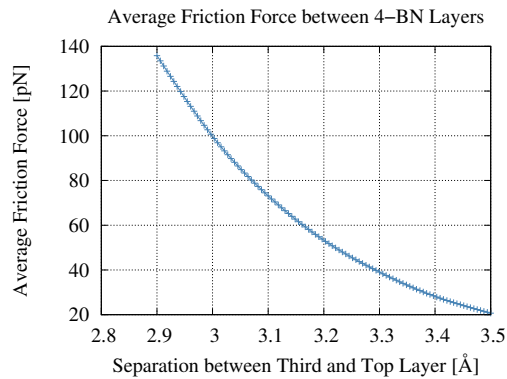


Figure 3.25: Average friction force at the interface of 4 layered h-BN/h-BN

rium distance of 2.99 \AA which is the same equilibrium distance between the second and the third layer. Then, the fifth layer has been placed and the calculations have

been performed while changing the vertical distance between the materials. The results are shown in Figure 3.27

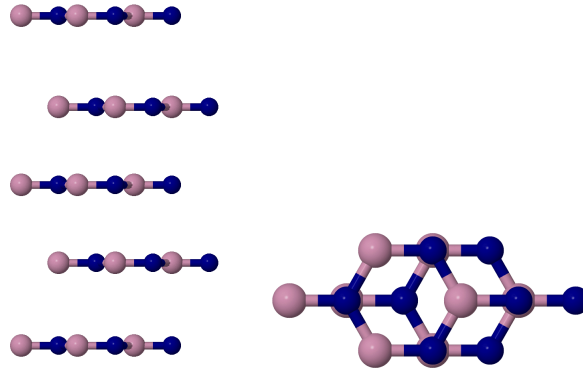


Figure 3.26: Five layered h-BN

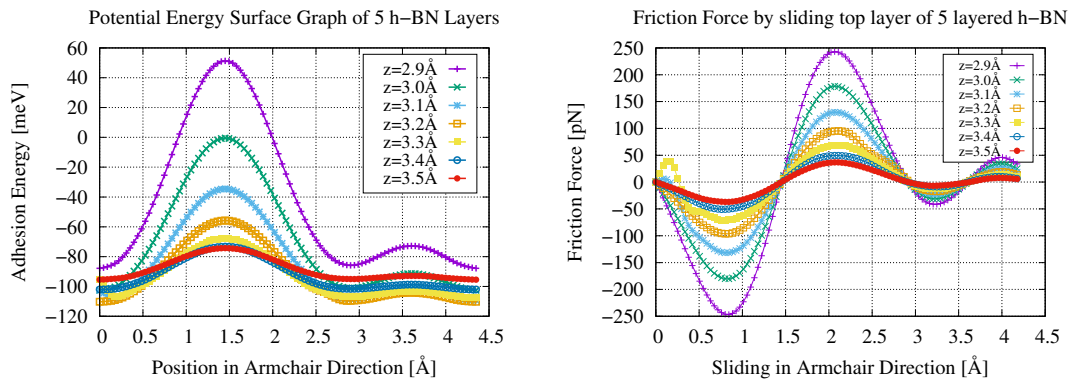


Figure 3.27: Adhesion energy and friction force at the interface of 5 layered h-BN/h-BN along x-direction

Once more, change in the average friction force with respect to the distance between fourth and the fifth layer is calculated and shown in Figure 3.28.

We have compared our average friction force findings of lamellar h-BN in Figure 3.29 and Table 3.3. It is seen that the number of h-BN layers from 2 to 5 affects the average friction. There seems to be a slight decrease in the trend. A similar study with molecular dynamics has been conducted by Suzhi et al. on graphene sheets sandwiched between amorphous silicon and AFM tip of Si under a constant load of 0.8 nN where they report that the average friction decreases as the number of graphene layers are increased [44]. This is explained by the size of the true contact

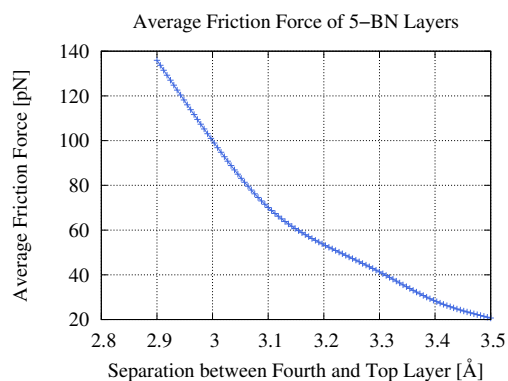


Figure 3.28: Average friction force at the interface of 5 layered h-BN/h-BN

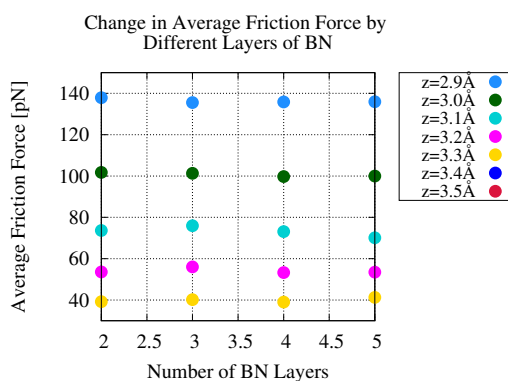


Figure 3.29: Average friction force vs number of h-BN layers

Table 3.3: Average Friction Force Change by the Number of Layers of the h-BN

| Change in Average Friction Force by Number of h-BN Layers | | | | | | | |
|---|--------|--------|--------|--------|--------|--------|--------|
| Number of BN layers | z=2.9Å | z=3.0Å | z=3.1Å | z=3.2Å | z=3.3Å | z=3.4Å | z=3.5Å |
| 2 | 137.90 | 101.73 | 73.63 | 53.60 | 39.22 | 28.17 | 20.77 |
| 3 | 135.52 | 101.31 | 75.95 | 56.02 | 40.21 | 29.64 | 21.94 |
| 4 | 135.84 | 99.74 | 73.11 | 53.30 | 39.04 | 28.17 | 20.67 |
| 5 | 135.93 | 99.96 | 70.11 | 53.48 | 41.29 | 28.29 | 20.69 |

area which is larger for thinner surfaces since the puckering effect becomes more observable. This is related to the bending stiffness of the sheet due to the out-of-plane deformation created by the movement of the tip. In their study, the decrease in the average friction is seen clearer due to the usage of a finite tip. The results of our

study are not as drastic as theirs since instead of a finite tip, an infinite sheet of BN has been used. Therefore, one cannot expect major differences in average friction force as the number of layer increases since puckering effect may not be as observable as for an infinite sheet unlike the case for a finite tip. The observed slight difference in our results is due to the vdW forces which are small. In addition, puckering effect also evolves with time and an eye-ful outcome of this phenomenon cannot be possible in static DFT calculations.

In another study conducted by Lee et al. with friction force microscopy (FFM), a decrease in the friction force when the number of h-BN layers is increased from single layer to four has been observed and this observation was attributed to the increase in the real contact area due to the puckering effect [27].

The change in average friction force between multi-layered h-BN is also explained by the change in the interlayer distances due to the important contribution of vdW dispersive interactions including Pauli repulsion in addition to the electrostatic interactions. The contribution of the vdW and the electrostatic interaction potentials are different for different stacking configurations [13]. Hence, when we keep in mind the stacking, it can be seen from our results at Table 3.3 that there is a slight decrease in the average friction force on some results when the number of layers of h-BN increases.

CHAPTER 4

FRICITION INVESTIGATION OF Au(111) SURFACES AND GOLD CLUSTERS OVER TWO DIMENSIONAL HEXAGONAL BORON NITRIDE

4.1 Au(111)/h-BN Interface

In this chapter, we explore the tribological properties of the Au(111)/h-BN interface. This is a unique interface between a metal and a two-dimensional system with polar bonds and therefore exhibits a rich variety of physics.

In the preliminary calculations at chapter 2, lattice constant of Au was calculated to be 4.11 Å with the DFT parameters we have used. Creating the interface presents certain challenges since the compatibility between lattice spacing of any two materials are one of the crucial factors that affects the nanotribological properties of the interfaces.

The mechanism is based on the ability of top surface atoms to overcome the potential barrier which is created by the substrate i.e bottom surface atoms. If the lattice parameters of top and bottom surfaces are in coincidence with one other, the system is said to be commensurate so the upper surface atoms lock into the potential wells created by the substrate, makes the sliding of top layer difficult, resulting in a greater friction force. On the other hand, if the lattice parameters of the two materials does not match, then the system is said to be incommensurate so the atoms in the upper layer cannot fit to the potential wells of the lower layer. In these cases, structural lubricity is a common occurrence.

In order to model such interfaces in periodic computational tools, the usual practice is to apply compressive/tensile strain to one or both of the materials. Such a ma-

nipulation of the lattice constants may potentially affect the results since the friction forces at the interface are largely governed by the electronic density, which in turn depends on atomic positions. As a means of testing the extent of this effect, we first investigate the magnitude of friction in the presence of an extreme amount of strain at the interface. We then proceed with a reasonable model with a much reduce level of mismatch.

4.1.1 3 layered Au(111)/h-BN Interface: An Extreme Case Investigation

For the pursuit of creating as commensurate an interface as possible, a 3 layered Au(111) slab has been modeled using 2×2 conventional unit cell and placed over the infinite sheet of 2×2 BN first. The procedure is not straightforward to apply since the lattice parameters of the materials are different from each other. Hence, in order to place the materials one over another within periodic boundary conditions, either the lattice parameters of h-BN need to be extended or the lattice parameters of Au(111) needs to be contracted. In each case, one has to remember that a strain is introduced to the system. We have performed both of the methods and calculated the adhesion energy change at the interface during sliding.

First, 2×2 unit cell of BN was extended by 16% in order to fit it to the unit cell of 2×2 Au(111). Then one material is kept fixed while the other one is moved along x-direction. Since they are in relative motion, the adhesion energy and the friction force at the interface will not be affected by the choice of whether the h-BN or Au(111) is mobile.

Next, the 2×2 unit cell of Au(111) is contracted by 13.8% to fit it the unit cell of 2×2 h-BN. The adhesion energy as a function of the vertical distance graphs for both cases are shown in Figure 4.2.

As seen from the results, the adsorption energy is found to be negative when h-BN is extended whereas it is positive in the case of the contraction of the (2×2) Au(111). We have used the structure of the extended h-BN and contracted Au(111) while we were calculating their optimized energies and utilized those energies when we calculate the adsorption energy at the whole interfaces. In fact, this result shows us

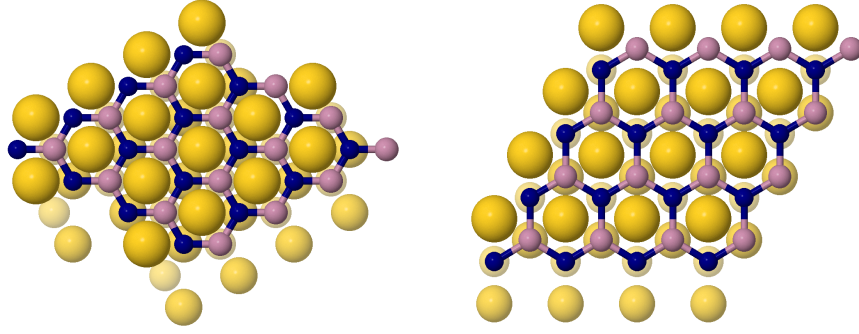


Figure 4.1: Left: (2×2) Au(111)- (2×2) BN when only Au(111) is contacted. Right: (2×2) Au(111)- (2×2) BN when only BN is extended. Pink color is for B atoms, blue is for N atoms and the yellow is for Au atoms where decreasing in size of the pale Au atoms indicates the relative distances from the uppermost h-BN.

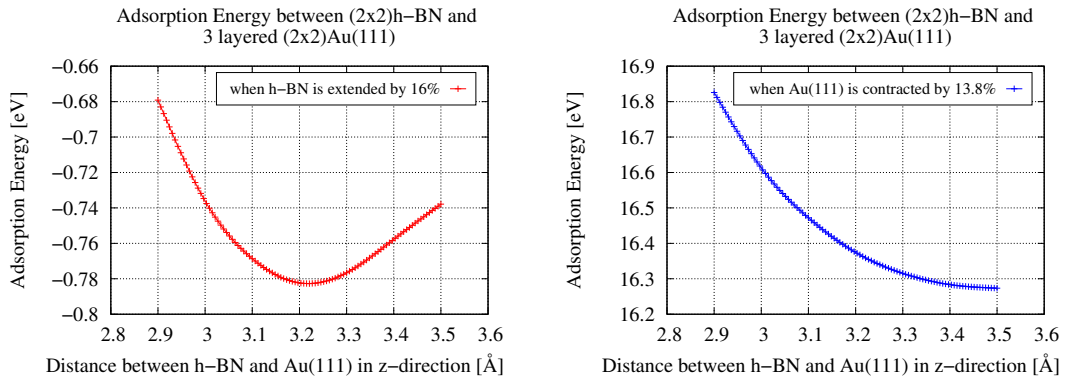


Figure 4.2: Adsorption energy at the interface of (2×2) Au(111)/ (2×2) h-BN. Left: when the h-BN is extended. Right: when the Au(111) is contracted.

(2×2) Au(111) cannot be contracted that much in order to place it over the (2×2) unit cell of BN, the results are extreme indeed. Due to its unstable nature, we discard the case with the positive adsorption energy here. Hence, only the friction force at the interface of the extended BN and the unchanged Au(111) is calculated. The results are shown in Figure 4.3.

Whereas in the case of Au under compressive strain, the adhesion energy is positive, in the case of BN extension, the adhesion energies are very strong. This is also reflected in the magnitude of lateral, friction forces, which are also large. We thus

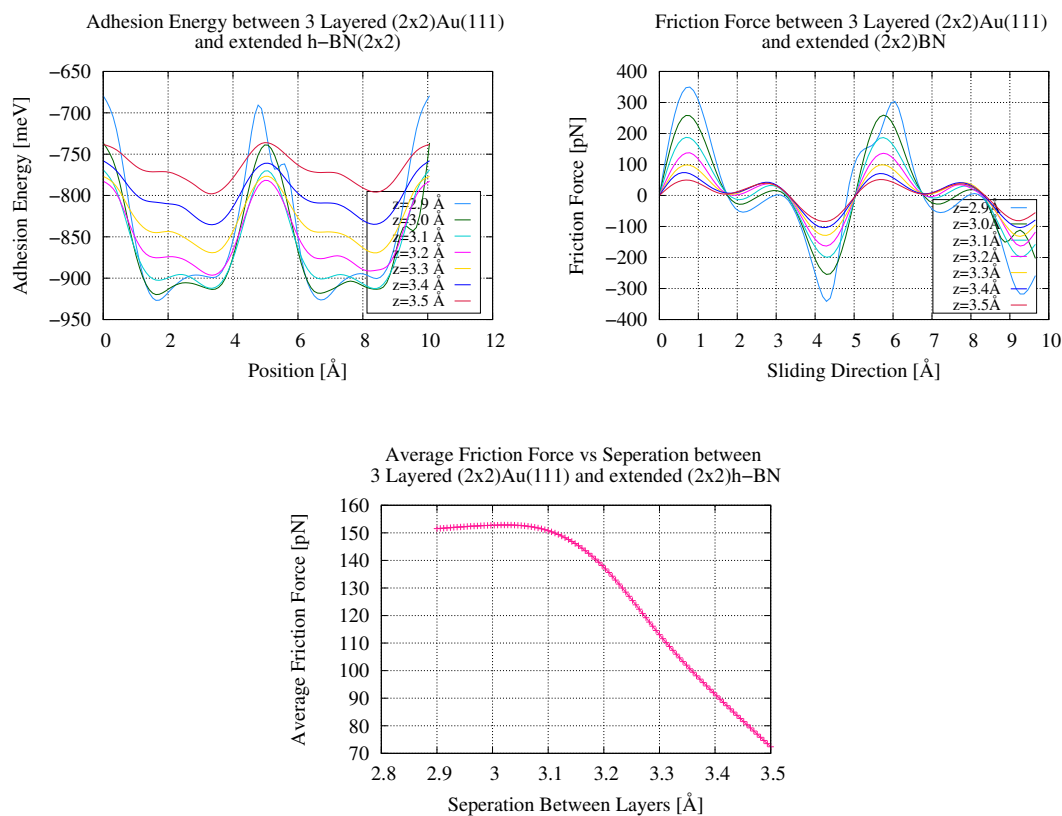


Figure 4.3: Adhesion energy and friction force at the interface of Au(111)/BN when BN is extended

conclude, by means of exploring its extreme limits that strain may indeed be a potential effect that needs to be factored in during the calculations regarding friction. Therefore, it should be minimized as much as is possible and practicable. At the very least, its effect should carefully be scrutinized.

4.1.2 4 layered Au(111)/h-BN Interface without the Strain

Convinced by the results of our investigation in the previous section that the strain introduced in the smaller simulation cell is prohibitively large, we employed a larger unit cell in an attempt to reduce the strain. The choice of 3×1 Au(111) and 2×2 h-BN indeed yields a perfect match with no need for compressive or tensile strain in either material. The rest of the calculations in this thesis will be performed using these supercells. (See Figure 4.4).

During the construction of the 4 layered Au(111), stacking of the layer construction has an effect on the interface properties. Hence, we have chosen to place the fourth layer of gold atoms so that the ABC stacking of the slab is preserved.

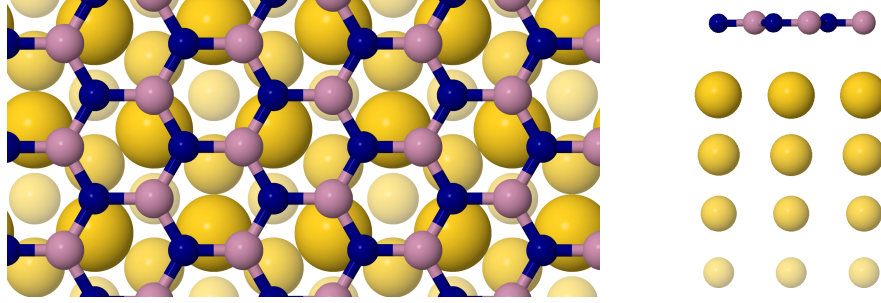


Figure 4.4: BN and Au(111) interface; unit cells are in perfect match. Pink, blue and yellow colors represent B, N and Au atoms respectively and the shrinking pale atoms is to represent the relative distance of the slab layers to the uppermost BN layer.

The adhesion energies for a variety of vertical separation have been calculated by subtracting the summation of the energies of the optimized geometries of (3×1) Au(111) and (2×2) h-BN from the total energy of the whole system as written in Equation 4.1.

$$E_{adh} = E_{system}^{total} - E_{(3 \times 1)Au111}^{opt} - E_{(2 \times 1)BN}^{opt} \quad (4.1)$$

Once the surface profile of the interface with the adhesion energy calculations is established, friction force of the system has been obtained at seven different vertical distances between 2.9 Å and 3.5 Å using the numerical derivative method as explained in the previous section. For the sake of simplicity, only the friction force results at 2.9 Å, 3.2 Å and 3.5 Å are shown in Figure 4.6. The average friction force as a function of the separation distance is also calculated and shown in Figure 4.6.

So far, we have the surface profile of the interface along x-direction, but we wish to obtain the full surface profile. Hence, we have moved the Au(111) over the h-BN sheet along every direction and obtained the potential energy surface (PES) of the 4 layered Au(111) and h-BN interface. (See Figure 4.7). The calculated adhesion energy is divided by four which corresponds to one h-BN unit so that the magnitude

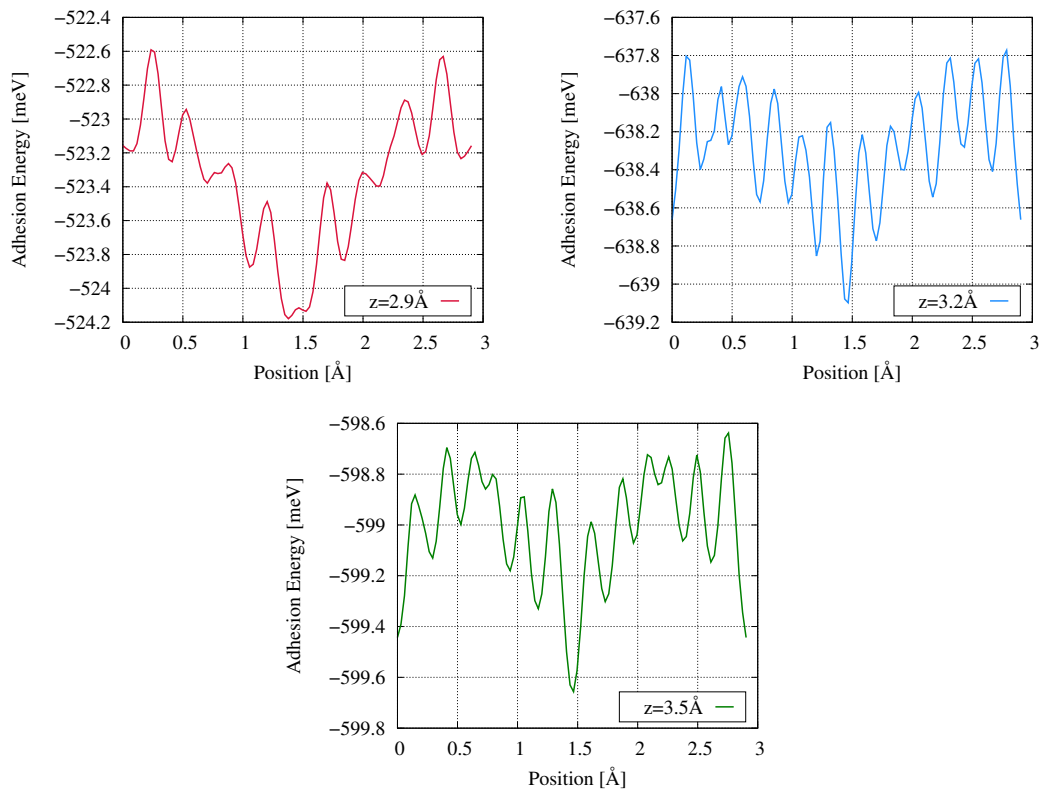


Figure 4.5: Adhesion energy at the interface of 4 layered Au(111)/h-BN, when moved along x-direction for different z-distances

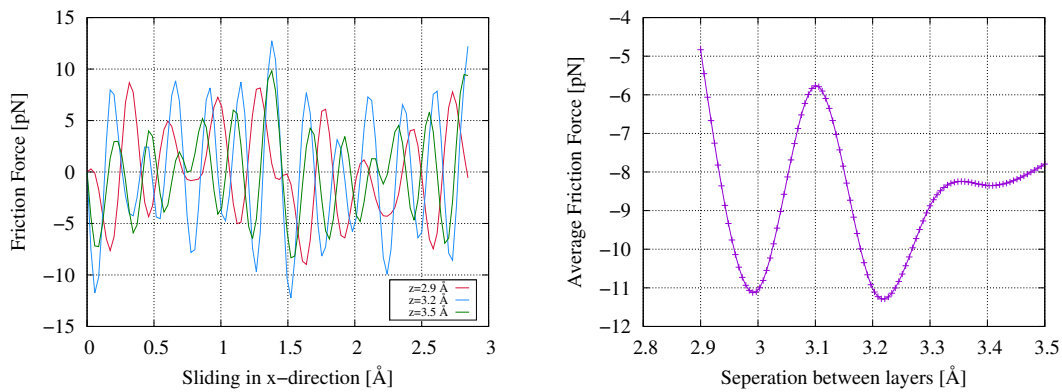


Figure 4.6: Friction force at the interface of 4 layered Au(111)/h-BN, when moved along x-direction for different z-distances

of the adhesion energy becomes comparable with the results of our previous and upcoming systems.

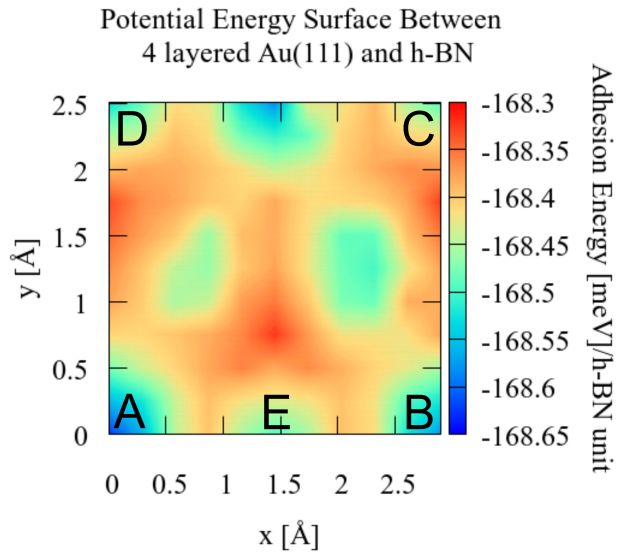


Figure 4.7: PES of 4 layered Au(111) and BN sheet.

The points labeled on PES are shown in the Figure 4.8.

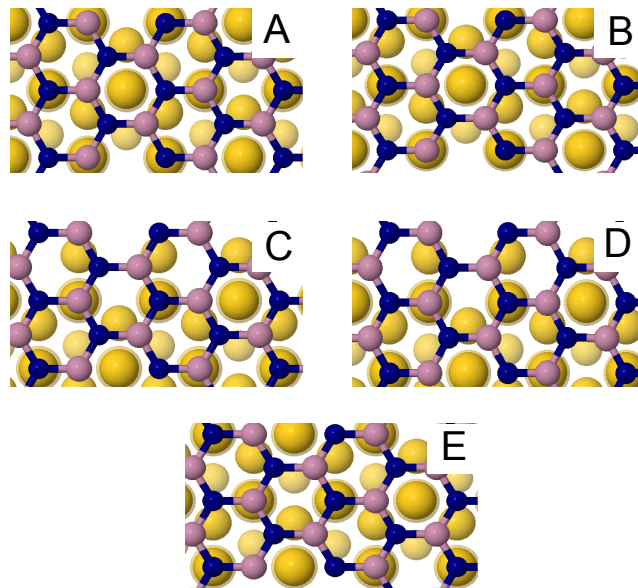


Figure 4.8: Relative positions during sliding as labeled on PES

From Figure 4.8, one can see that the locations labeled as A, B and E all correspond to the same atomistic arrangement during sliding. The atoms of h-BN and Au(111) are aligned so that the sliding steps of A, B and E are exactly identical. Similarly, positions C and D correspond to an equal arrangement.

4.2 Nanotribological Properties of the Au(111)/h-BN Interface Under Applied Load Force

We defined the load force in the previous chapter as any vertical position between two materials different than the equilibrium distance results in a vertical strain at the interface. This vertical strain is the load force and it depends on the distance between the tip and the surface. In chapter 3, nanotribological properties at the interface of h-BN/h-BN has been examined under the presence of the load and now, using the same methods and contact area estimation which was calculated to be $20,000 \text{ nm}^2$, Au(111)/h-BN interface will be investigated under the presence of the vertical load, as well. The procedure is exactly the same as in chapter 3. The area of the supercell we are using here is $0,219 \text{ nm}^2$ which means that we assume there are over 90,000 supercells at the contact of Au(111) coated AFM tip and the h-BN.

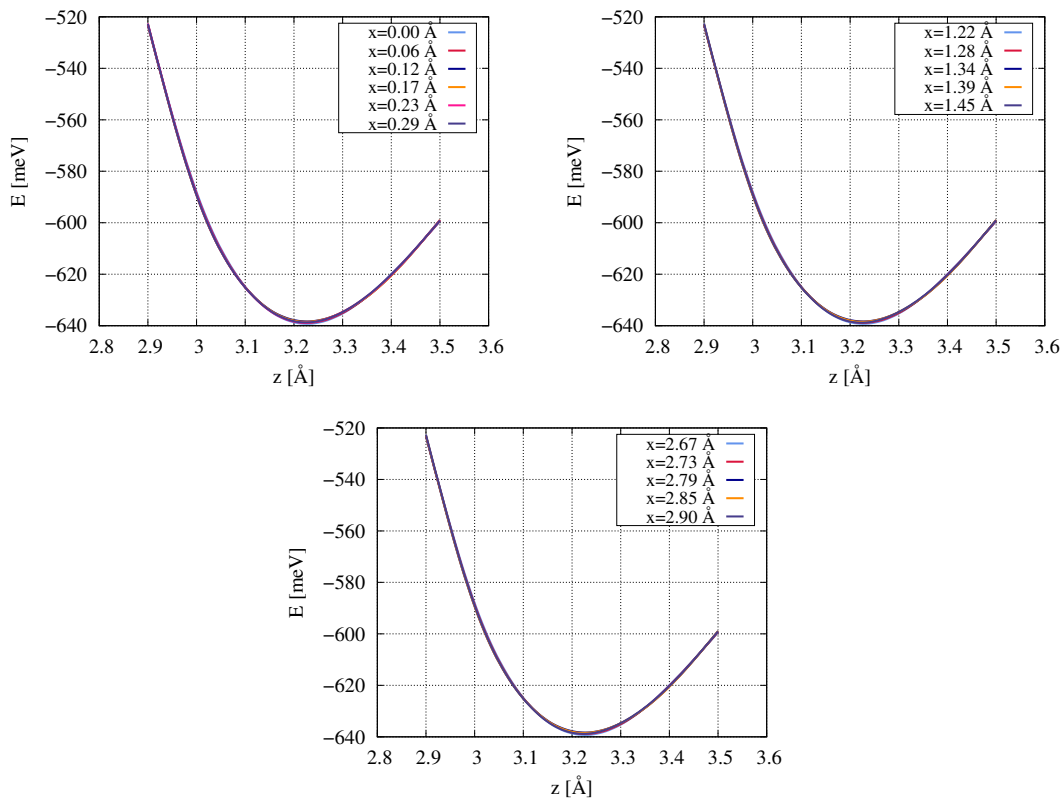


Figure 4.9: Adhesion energy as a function of separation distance between 4 layered Au(111) and BN at each lateral position

In order to decide the load force that we wish to apply to the interface here, first, adhesion energy as a function of the vertical distance at each lateral position of 0.06 \AA has been calculated with the similar method used in chapter 3, all the way through 2.90 \AA totaling to 50 steps of simulation. For the sake of simplicity, we have left out some intermediate steps of the results again and shown the rest of them at the three graphs corresponding to different lateral (x) positions as seen in Figure 4.9. Load force is found by taking the negative derivative of the total energy with respect to the vertical distance between the materials as shown in Equation 3.5.

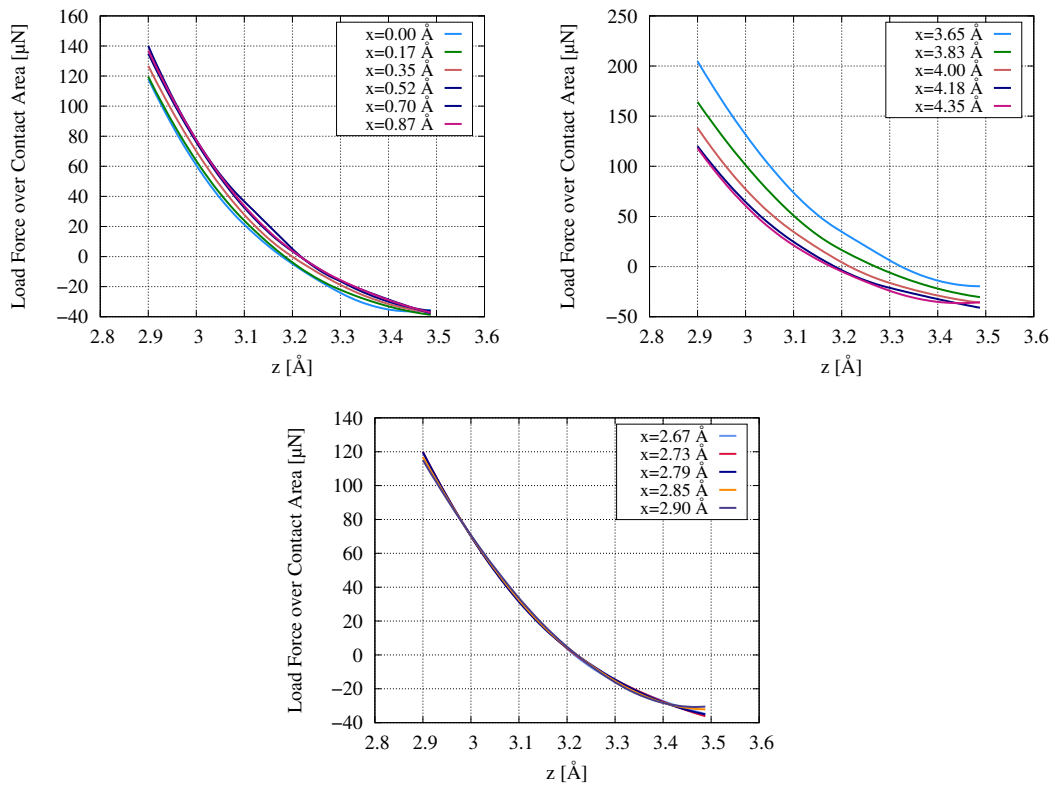


Figure 4.10: Load as a function of separation distance between 4 layered Au(111) and BN at each lateral position over the estimated contact area

The change in the adhesion energy at the interface during the motion along x-direction under the chosen vertical loads are calculated. The results are shown in Figure 4.11.

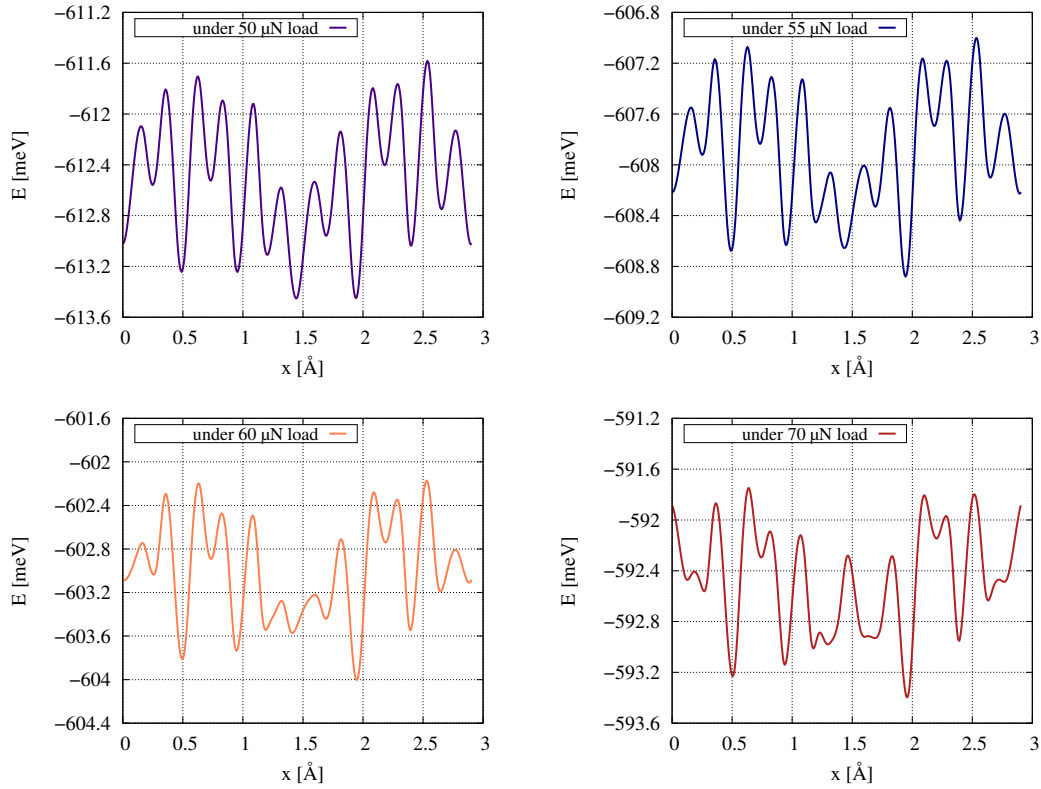


Figure 4.11: Adhesion energy at the interface of 4 layered Au(111) and h-BN under several magnitudes of normal load

The friction force is calculated by using the numerical derivative of the energy and the results are shown in Figure 4.12 along with the average friction force and the friction coefficients as reported in Table 4.1 where the load and the average friction force over one h-BN unit has also been calculated and shown in Table 4.1 to be able to make a comparison with the other results of our research.

As an attempt to understand the electronic origins of the tribological behavior, the average charge density difference along the vertical distance at the Au(111)/BN interface under the normal load of $50 \mu\text{N}$ and $70 \mu\text{N}$ have been calculated at the lateral positions of $x=0$ and $x=1.5 \text{ \AA}$ and shown in Figure 4.14. At first glance, the charge density difference profile in both cases are very similar. The charge profile of the interface is interesting. It is polarized with an electron excess in the Au side and a deficiency in the BN side of the interface. While the Au surface remains more or less neutral, the BN sheet appears to have been charged positively. Due to the high

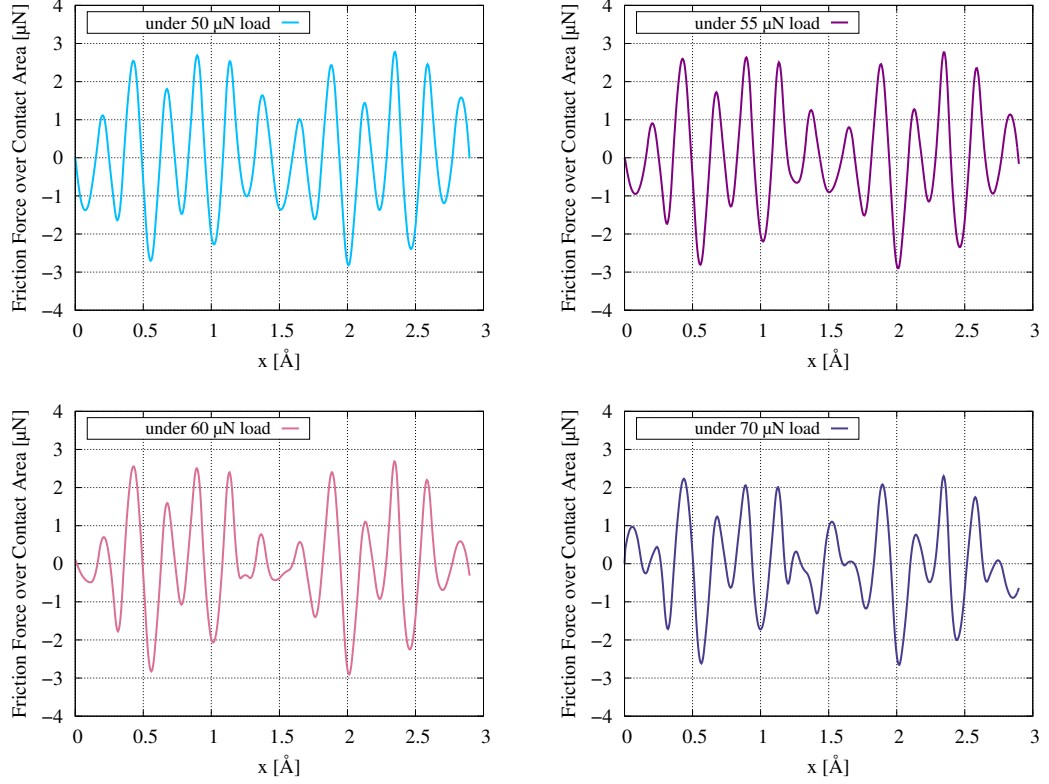


Figure 4.12: Friction force at the interface of 4 layered Au(111) and BN under applied normal force

Table 4.1: Friction coefficient and average friction force between 4 layered Au(111) and h-BN. The results are shown with and without the contact area.

| Friction Coefficient (μ) and F_{average} under vertical loads (N) | | | | |
|--|----------------------------------|--|--|-------|
| Load [μN] | Load per BN unit [$n\text{N}$] | F_{average} [μN] | F_{average} per BN unit [$n\text{N}$] | μ |
| 50 | 0.14 | 1.19 | 0.013 | 0.024 |
| 55 | 0.15 | 1.09 | 0.012 | 0.020 |
| 60 | 0.16 | 0.94 | 0.010 | 0.016 |
| 70 | 0.19 | 0.92 | 0.010 | 0.013 |

lubricity of this interface as understood from our results, the average charge density difference with the presence of the different magnitudes of load does not change significantly as well as with the different lateral positions.

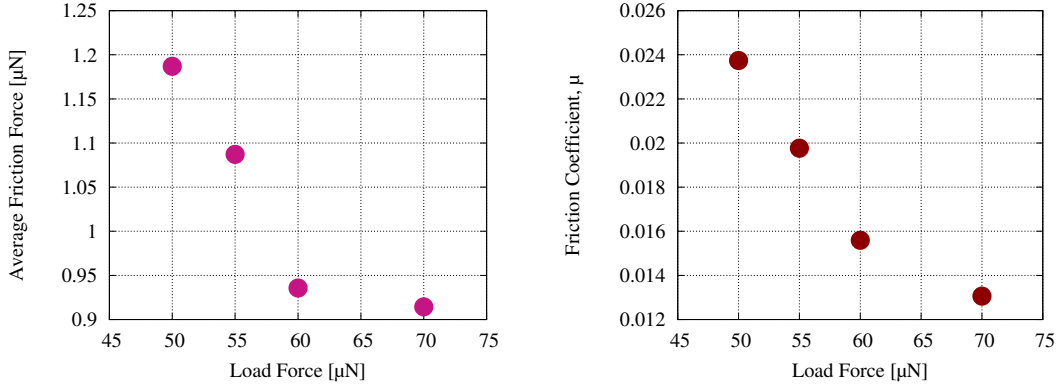


Figure 4.13: Average friction force and the friction coefficient as a function of load at the interface of 4 layered Au(111)/h-BN

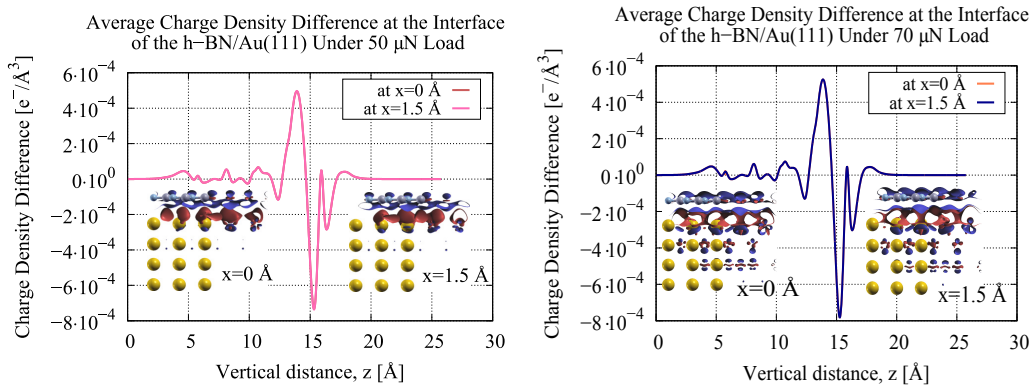


Figure 4.14: Average charge density difference at different lateral (x) position between Au(111) and h-BN

4.3 Gold Clusters and h-BN

Au nano clusters are of interest due to their potential applications in technology [50]. Since they demonstrate many different geometries, properties of the clusters highly depend on its shape and the size. In literature, there are several studies showing the stability of the Au clusters depending on the size and the geometry [42, 46, 49, 52]. Even for a given certain number of atoms, Au clusters may vary their structure due to entropic and dynamic effects [10]. Since their interaction with materials are also expected to be different than that of their bulk structures, they are needed to be examined in order to see especially the edge effects of the tip in AFM/FFM experiments.

In this thesis, one Au atom, rhombic Au cluster consisting of 4 gold atoms and icosahedral Au cluster with 13 atoms are placed over BN sheet and nanotribological properties of the systems are examined.

4.3.1 Au atom over h-BN

A benchmark calculation has been performed using one Au atom placed over an infinite sheet of (3×3) BN. Potential energy surface of the interface are calculated and the resulting map is shown in Figure 4.15 along with the starting configuration. From the PES, one can see the places where Au atom is energetically the most and the least favorable. The middle region of the PES indicates the least stable configuration where Au atom is aligned with the B-atom of the h-BN. The adhesion energy and the average friction for the zigzag sliding direction of the Au atom on the BN sample has been investigated and the results are shown in Figure 4.16. For the adhesion energy calculations in Figure 4.16, the z-coordinate of the atoms is allowed to be relaxed while performing DFT, so, there is no vertical load between the Au atom and the h-BN. Friction force at the interface is calculated with the same method as before, and its average value has been found to be 76.27 pN as shown inside the friction force graph in Figure 4.16. The average friction force of this system at zero load is very large compared to the Au(111)/h-BN interface whose average friction was found to be 0.013 nN (13 pN) with the presence of the load. Therefore, the average friction of one gold atom and BN sample has at least five times larger than that of the Au(111)/BN interface while the magnitude of the adhesion energy is greater as well compared to the results of adhesion energy per BN-unit shown in Figure 4.7.

4.3.2 Rhombic Au over h-BN

The most stable structure of Au_4 clusters examined in several studies. It has been shown that with 4-atoms Au clusters, monoatomic zigzag or linear nanowire, rhombus shape, Y-shape or square shape clusters can be obtained and for a clean Au_4 , rhombus shape has the lowest energy so it is the most stable one [46]. In our study, nanotribological properties of the rhombic Au_4 has been studied.

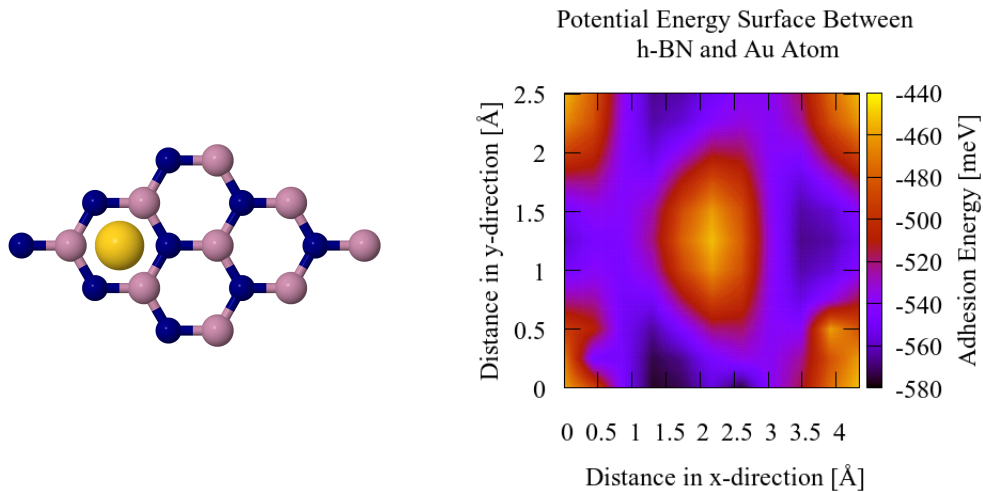


Figure 4.15: Potential energy surface at the interface of Au atom and h-BN (right) along with the starting configuration (left).

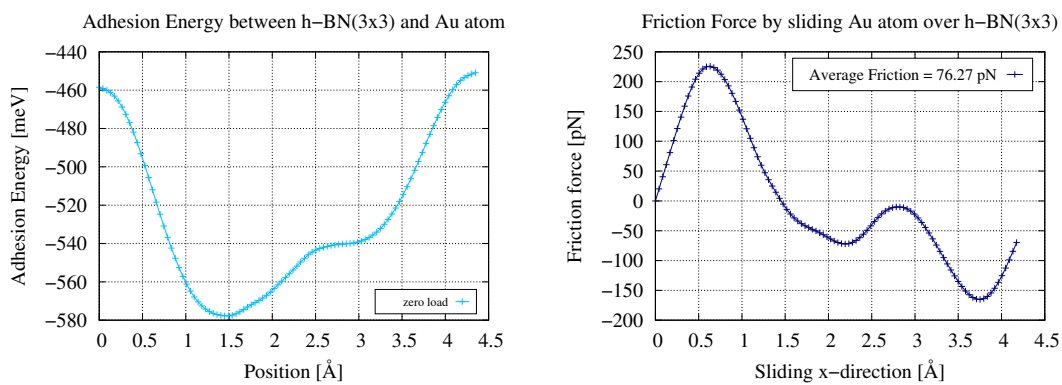


Figure 4.16: Adhesion Energy Graph of Au atom over (3x3)BN sheet

During the structure optimization, it was observed that the Au₄ structure tilted due to the existence of vdW forces. This optimization has been done using several unit cell sizes to make sure that the interaction between the two consecutive simulation boxes are eliminated. Once we have chosen a large enough unit cell of 4×4 , friction forces during sliding for both the tilted and the flat clusters were calculated in order to understand the effect of this tilting. The results are shown in Figure 4.17 and the average friction values are indicated inside of the graphs. We have seen that the tilted cluster strongly interacts with the BN sample via one atom at the bottom so the adhesion energy at the interface is very large compared to the planar case.

Accordingly, average friction is larger for the tilted cluster case as seen.

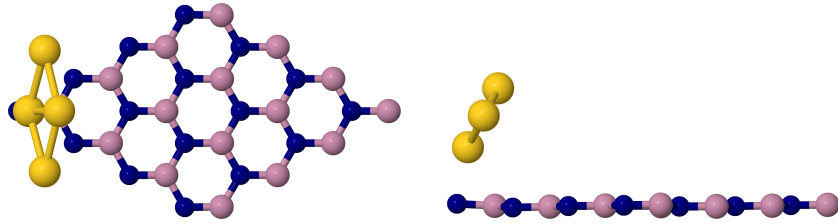


Figure 4.17: Au_4 is placed over (4×4) BN; top view and side view

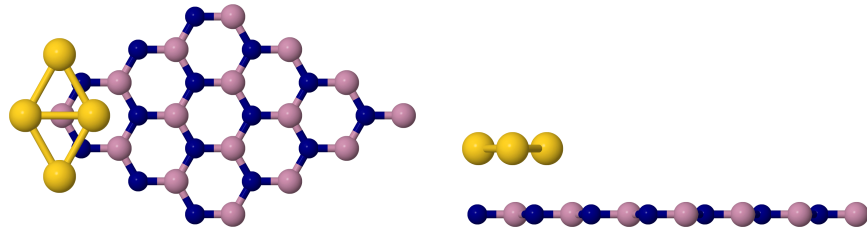


Figure 4.18: Au_4 is placed over (4×4) BN when it is kept planar by force; top view and side view

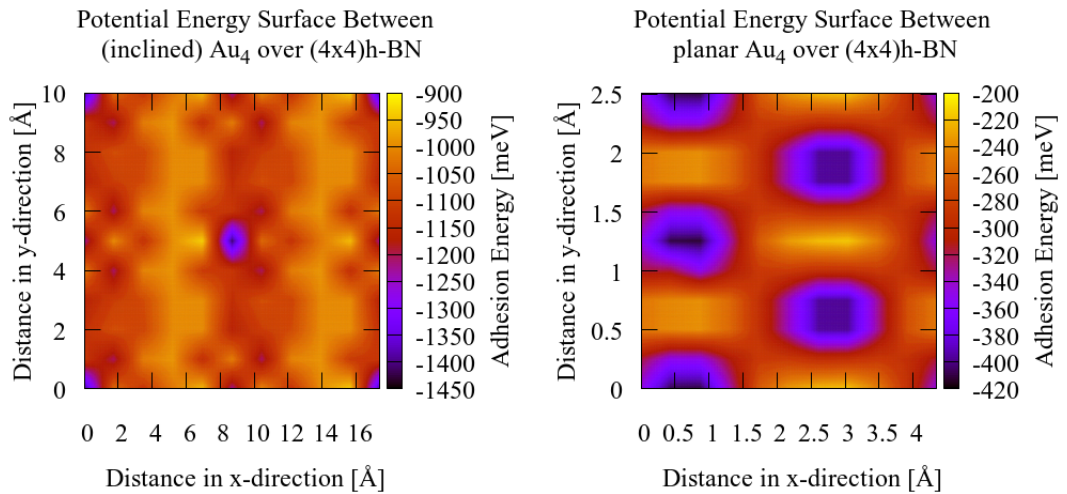


Figure 4.19: Au_4 over (4×4) BN PES graphs; top: Tilted Au_4 , bottom: Planar Au_4

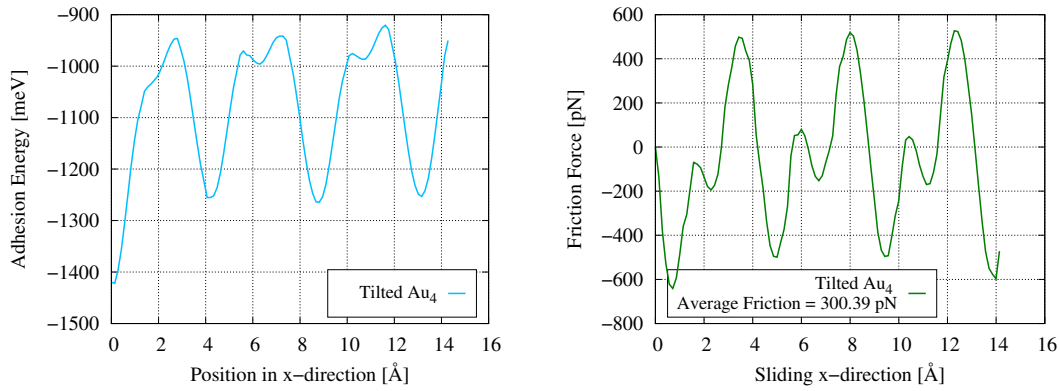


Figure 4.20: Adhesion energy and friction force of Rhombic Au (Au_4) over BN (tilted configuration)

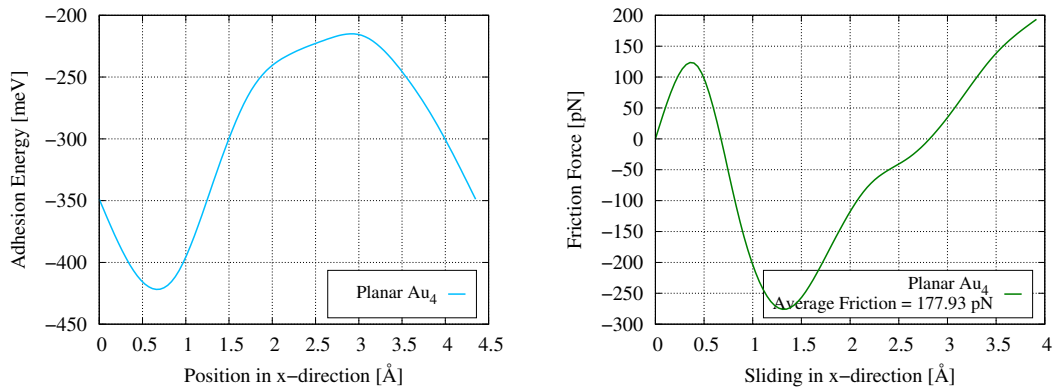


Figure 4.21: Adhesion energy and friction force of Rhombic Au (Au_4) over BN (planar configuration)

4.3.3 Icosahedral Au_{13} over h-BN

As the number of atoms in a cluster increases, the number of possible local minima of its configurations also increase. For this reason, we conducted an extensive literature search to identify the most likely configuration for the Au_{13} cluster. In [43], Shafai et al. examine Au_{13} cluster and performed a constant temperature molecular dynamics to obtain the relaxed geometries after generating the initial structure of the cluster. After finding a number of geometries of Au_{13} , they proceed with the DFT calculations to find the most stable structures. Among each type of clusters, they choose planar, flake, cub-octahedral and icosahedral structures. In their study, it is shown that for

the clean Au_{13} cluster, planar structure is the most stable one among others while the icosahedral is the least stable. This is supported by another study conducted by Xiao et al [49] which also shows that the zigzag monoatomic gold clusters are more stable than the linear monoatomic gold clusters. An important point worth mentioning is that the icosahedral structure undergoes a Jahn-Teller distortion due to the degenerate states of the highly symmetric structure and therefore, collapses to the distorted cuboctahedral geometry as shown in [43]. In another study conducted by Wang et al. [46], it is reported that the lowest energy configuration of Au_{13} cluster is neither icosahedron nor cuboctahedron but an amorphous structure as it is compatible with the result of Shafai et al. [43]. Shafai et al. [43] also noted that for the ligated Au_{13} cluster, planar structure is no more the energetically favorable one. In fact, the energetic order is reversed for the ligated case of Au_{13} where this time (distorted) icosahedral structure become the most stable one.

In several studies, 13-atoms Au cluster is pinpointed as the transition point from 2D to 3D structures [17,49]. Up to 13 atoms, Au clusters favor a planar shape and make a transition to the 3D shape for larger sizes. In this thesis, icosahedral structure of Au_{13} cluster is placed over h-BN to understand the size effect on nanotribology by means of studying a larger cluster.

Perfect structure of icosahedral and cuboctahedral Au clusters are shown in Figure 4.22 and they have been constructed by using the space vectors given in chapter 2.

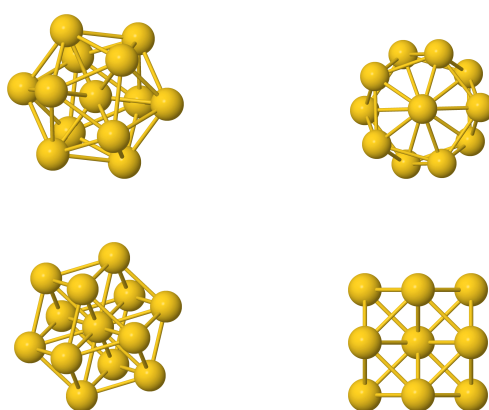


Figure 4.22: Perfect icosahedral (top row) and perfect cuboctahedral (bottom row) from side and top view

Icosahedral cluster which consists of 13-atoms has been placed over infinite sheet of h-BN. In order to eliminate the interaction between the Au clusters inside the consecutive simulation boxes, the supercell size of 6×6 BN has been chosen to construct the interface properly. Next, the geometry optimization of the Au₁₃/h-BN system was performed to obtain the most stable structure. The result of the geometry optimization revealed that there is a structural transition from perfect icosahedral to distorted cuboctahedral. This result is compatible with the literature. The structural transition from perfect icosahedral to distorted cuboctahedral is due to the high symmetry of the icosahedron as discussed earlier in this section. Therefore, the remaining calculations have been performed using this configuration of distorted cuboctahedral, so, distorted cluster has been moved over the h-BN. The results are shown in Figure 4.24

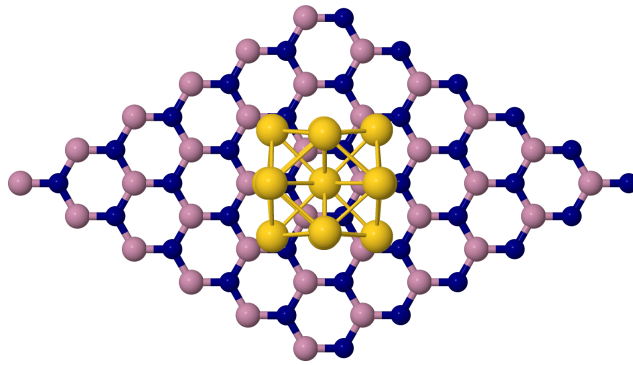


Figure 4.23: Structural transition from perfect icosahedral to distorted cuboctahedral when Au₁₃ is placed over BN sample.

The average friction force has been calculated to be 204.88 pN over the one unit cell as also shown inside the friction graph. This is a very large value compared to the previous systems of h-BN/h-BN and Au(111)/h-BN interfaces if their results are considered over one unit cell instead of a whole contact area. This is due to the increase in the unsaturated electrons at the edges of the clusters. The average friction force of the Au₁₃ and BN interface is much larger than the case of one Au atom. However, although it is smaller than the average friction of the rhombic Au cluster case, there is not a major difference. Average friction of the Au₁₃ with BN was calculated to be about 204 pN whereas it is about 300 pN for the tilted rhombic Au cluster case. In both of the systems, the adhesion energy at the interface is larger than that of the previous systems but it is even larger for Au₁₃. The Au₁₃ cluster strongly

interacts with the BN, almost covalently bonding and the corrugation is extensive.

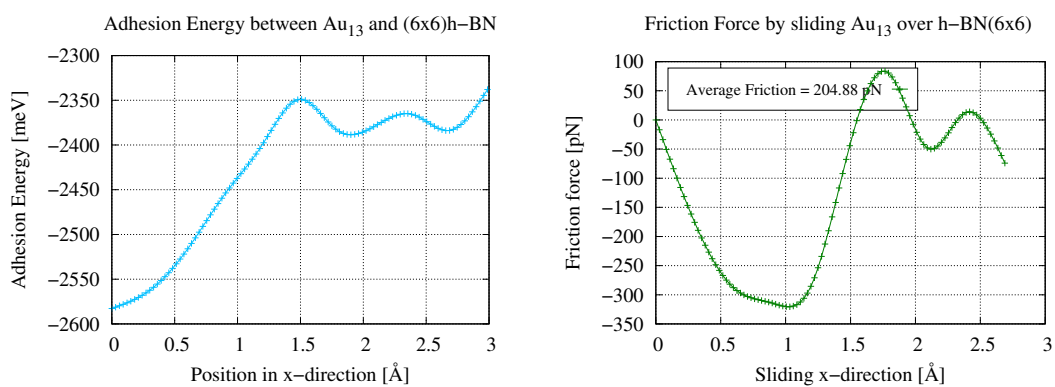


Figure 4.24: Adhesion energy and friction force of icosahedral Au₁₃ over h-BN

In the next chapter, we will further discuss our results and make a summary.

CHAPTER 5

CONCLUSION AND DISCUSSION

In this thesis, we have examined the nanotribological properties of the different interfaces by modeling them using Density Functional Theory (DFT).

First, we have investigated the tribological behavior of the h-BN/h-BN interface along zigzag and armchair directions while changing the vertical distance. We have seen that the maximum average friction force value is obtained when we slide one layer along the armchair direction due to the repeated ontop-ontop coincidence of the same atoms between the upper and the lower layer. In addition, we have seen that the friction force becomes smaller when we increase the vertical distance between the materials from 2.9 Å to 3.2 Å where the equilibrium distance between the two is around 3.2 Å at the initial point and varies a little during the sliding path. Average friction forces and friction coefficients under different magnitudes of vertical load have also been investigated and it is found that the average friction force increases with the increase in the vertical load for this system.

We have also investigated the friction force at the interface of the h-BN/h-BN when we increase the number of h-BN layers. An increase in the number of layers results in a small decrease in the friction force.

Next, the Au(111)/h-BN interface and the interaction between gold clusters and h-BN have been investigated. The Au(111)/h-BN interface was examined under several magnitudes of normal load and average friction forces and friction coefficients were calculated. The average friction force at the interfaces become smaller if the commensurability of the system decreases. The Au(111)/h-BN interface is incommensurate compared to the h-BN/h-BN interface. Hence, the average friction force per unit cell

and the friction coefficient itself are found to be small. Even under an applied normal force, the interface reveals possible superlubric behavior due to the small values of the friction coefficient. The friction coefficients for the Au(111)/h-BN interface are close to the range of the numbers that are used in the definition of the superlubricity [33]. For instance, under an applied normal load of $70 \mu\text{N}$ over our estimated contact area, which corresponds to 0.19 nN per BN unit, friction coefficient was calculated to be 0.013. On the other hand, friction coefficient under this load for h-BN/h-BN interface has been found to be 0.17. The friction coefficient between two sliding wood is about 0.2 just a reminder to the reader in order to be able to make a comparison.

In the case of the clusters, the commensurability of the interface consisting of clusters and the h-BN is high causing the friction force to be much larger compared to the h-BN/h-BN and Au(111)/h-BN interfaces.

We have seen that the friction force is connected to the corrugation of our systems. Corrugation here is defined as the difference between the maximum and the minimum adhesion energy on the potential energy surface. The corrugation of the potential energy surface of the Au(111)/h-BN interface was calculated, and the energy values have been converted to one h-BN unit so that we can compare it with the result of h-BN/h-BN interface. We have found that the maximum value of the corrugation at the Au(111)/h-BN interface under no load is 0.35 meV which is very small, so is the average friction force being 0.49 pN at zero load. Corrugation of the h-BN/h-BN interface along armchair direction at zero load is about 34.42 meV which is two order of magnitude larger than that of the Au(111)/h-BN interface and the average friction at this interface at zero load is calculated to be 31.72 pN .

When we look at the corrugation of the gold clusters-h-BN interfaces, the magnitude of the minimum and the maximum adhesion energy differences are even larger, in the range of several hundred meV, making a huge difference between the previous systems. It is about 140 meV for one gold atom, 220 meV and 550 meV for planar and tilted rhomboid gold clusters respectively and 245 meV for icosahedral Au cluster system at the contact of h-BN sample. The average friction forces are calculated to be 76 pN for one gold atom, 178 pN and 300 pN for planar and tilted rhombic gold cluster cases respectively and 205 pN for icosahedral Au cluster system. These results

which show the increase in the corrugation causes increase in the friction force are consistent with the study of Wolloch et al. [48].

In summary, we have seen that the Au(111)/h-BN interface reveals superlubric-like behavior since the friction coefficient of the system is close to the range of the friction coefficients that are used for the definition of the superlubricity even with the presence of an load. We have also seen that the commensurability of the system while constructing has an impact on the nanotribological behavior of the system. The friction force between Au clusters and h-BN is much larger than that of the bulk Au and h-BN, leading to an increase in the overall friction of the systems. Finally, static calculations that we report here indicate an upper limit to the static friction and our results will be a benchmark for the future AFM/FFM experiments.

REFERENCES

- [1] M. Allen, H. Sumali, and P. C Penegor. Effect of tip mass on atomic force microscope calibration by thermal method. *Conference Proceedings of the Society for Experimental Mechanics Series*, 01 2009.
- [2] M. Z. Baykara, M. R. Vazirisereshk, and M. Ashlie. Emerging superlubricity: A review of the state of the art and perspectives on future research. *Applied Physics Reviews*, 5(041102), 2018.
- [3] K. Berland, V. R. Cooper, K. Lee, E. Schröder, T. Thonhauser, P. Hyldgaard, and B. I. Lundqvist. van der waals forces in density functional theory: a review of the vdw-df method. *Reports on Progress in Physics*, 78(6), 2015.
- [4] B. Bhushan. *Modern Tribology Handbook, Two Volume Set*, volume 1. CRC Press, 2000.
- [5] B. Bhushan. *Nanotribology and Nanomechanics*. Springer, 2008.
- [6] B. Bhushan and A. Kulkarni. Effect of normal load on microscale friction measurements. *Thin Solid Films*, 278:49–56, 1996.
- [7] G. C. Bond. Gold: a relatively new catalyst. *Catalysis Today*, 72(1):5 – 9, 2002. Catalytic Gold 2002.
- [8] V. R. Cooper. Van der waals density functional: An appropriate exchange functional. *Phys. Rev. B*, 81:161104, Apr 2010.
- [9] M. Dienwiebel, G. S. Verhoeven, N. Pradeep, J. W. M. Frenken, J. A. Heimberg, and H. W. Zandbergen. Superlubricity of graphite. *Phys. Rev. Lett.*, 92:126101, Mar 2004.
- [10] J. P. K. Doye and F. Calvo. Entropic effects on the size dependence of cluster structure. *Phys. Rev. Lett.*, 86:3570–3573, Apr 2001.

- [11] M. Enachescu, R. Van den Oetelaar, R. Carpick, C. Flipse, and M. Salmeron. Observation of proportionality between friction and contact area at the nanometer scale. *Tribology Letters*, 7:73–78, 1999.
- [12] A. Erdemir and J.-M. Martin. Introduction. In A. Erdemir and J.-M. Martin, editors, *Superlubricity*, pages xvii – xix. Elsevier Science B.V., Amsterdam, 2007.
- [13] W. Gao and A. Tkatchenko. Sliding mechanisms in multilayered hexagonal boron nitride and graphene: The effects of directionality, thickness, and sliding constraints. *Phys. Rev. Lett.*, 114:096101, Mar 2015.
- [14] P. Giannozzi, O. Andreussi, T. Brumme, O. Bunau, M. B. Nardelli, M. Calandra, ..., and S. Baroni. Advanced capabilities for materials modelling with quantum espresso. *Journal of Physics: Condensed Matter*, 29(46):465901, 2017.
- [15] P. Giannozzi, S. Baroni, N. Bonini, M. Calandra, R. Car, C. Cavazzoni, ..., and R. M. Wentzcovitch. Quantum espresso: a modular and open-source software project for quantum simulations of materials. *Journal of Physics: Condensed Matter*, 21(39):395502 (19pp), 2009.
- [16] F. Giustino. *Materials Modelling using Density Functional Theory*. Oxford, 2014.
- [17] M. Gruber, G. Heimel, L. Romaner, J.-L. Brédas, and E. Zojer. First-principles study of the geometric and electronic structure of Au_{13} clusters: Importance of the prism motif. *Phys. Rev. B*, 77:165411, Apr 2008.
- [18] M. Hirano and K. Shinjo. Atomistic locking and friction. *Phys. Rev. B*, 41:11837–11851, Jun 1990.
- [19] M. Hirano and K. Shinjo. Superlubricity and frictional anisotropy. *Wear*, 168(1):121 – 125, 1993.
- [20] P. Hohenberg and W. Kohn. Inhomogeneous electron gas. *Phys. Rev.*, 136:B864–B871, Nov 1964.

- [21] M. Hu, Z. Yu, J. Yin, C. Zhang, and L. Sun. A dft-lda study of electronic and optical properties of hexagonal boron nitride under uniaxial strain. *Computational Materials Science*, 54:165 – 169, 2012.
- [22] T. Jacobs and A. Martini. Review : Measuring and understanding contact area at the nanoscale. *Applied Mechanics Reviews*, 69, September 2017.
- [23] R. O. Jones and O. Gunnarsson. The density functional formalism, its applications and prospects. *Rev. Mod. Phys.*, 61:689–746, Jul 1989.
- [24] W. Kohn and L. J. Sham. Self-consistent equations including exchange and correlation effects. *Phys. Rev.*, 140:A1133–A1138, Nov 1965.
- [25] J. Krim. Friction and energy dissipation mechanisms in adsorbed molecules and molecularly thin films. *Advances in Physics*, 61(3):155–323, 2012.
- [26] S. Y. Krylov and J. W. M. Frenken. The physics of atomic-scale friction: Basic considerations and open questions. *physica status solidi (b)*, 251(4):711–736, 2014.
- [27] C. Lee, Q. Li, W. Kalb, X. Liu, H. Berger, R. Carpick, and J. Hone. Frictional characteristics of atomically thin sheets. *Science (New York, N.Y.)*, 328:76–80, 04 2010.
- [28] D. Leidermark. Modelling of constitutive and fatigue behaviour of a single-crystal nickel-base superalloy. 06 2010.
- [29] O. Leung and M. Goh. Orientational ordering of polymers by atomic force microscope tip-surface interaction. *Science*, 255:64–66, 1992.
- [30] H. Li, J. Wang, S. Gao, Q. Chen, L. Peng, K. Liu, and X. Wei. Superlubricity between MoS₂ monolayers. *Advanced Materials*, 29, May 2017.
- [31] S.-W. Liu, H.-P. Wang, Q. Xu, T.-B. Ma, G. Yu, C. Zhang, ..., and J. Luo. Robust microscale superlubricity under high contact pressure enabled by graphene-coated microsphere. *Nature Communications*, (14029), February 2017.
- [32] B. I. Lundqvist, Y. Andersson, H. Shao, S. Chan, and D. C. Langreth. Density functional theory including van der waals forces. *International Journal of Quantum Chemistry*, 56(4):247–255, 1995.

- [33] J. M. Martin and A. Erdemir. Superlubricity: Friction's vanishing act. *Physic Today*, 71:40, 2018.
- [34] I. Mayer. *The Hartree-Fock Method*, pages 165–225. Springer US, Boston, MA, 2003.
- [35] M. McGuigan and J. W. Davenport. Computational exploration of the nanogold energy landscape. 12 2009.
- [36] M. H. Müser. Atomistic simulations of solid friction. In P. Nielaba, M. Mareschal, and G. Ciccotti, editors, *Bridging Time Scales: Molecular Simulations for the Next Decade*, pages 289–317. Springer Berlin Heidelberg, Berlin, Heidelberg, 2002.
- [37] T. Onodera, Y. Morita, R. Nagumo, R. Miura, A. Suzuki, H. Tsuboi, ..., and A. Miyamoto. A computational chemistry study on friction of h-MoS₂. part ii. friction anisotropy. *The Journal of Physical Chemistry B*, 114(48):15832–15838, 2010. PMID: 21077588.
- [38] Q. Peng, W. Ji, and S. De. Mechanical properties of the hexagonal boron nitride monolayer: Ab initio study. *Computational Materials Science*, 56:11 – 17, 2012.
- [39] J. P. Perdew, K. Burke, and M. Ernzerhof. Generalized gradient approximation made simple. *Phys. Rev. Lett.*, 77:3865–3868, Oct 1996.
- [40] C. Rajesh, S. Nigam, and C. Majumder. The structural and electronic properties of Au_n clusters on the $\alpha - Al_2O_3(0001)$ surface: a first principles study. *Phys. Chem. Chem. Phys.*, 16:26561–26569, 2014.
- [41] M. Reguzzoni, A. Fasolino, E. Molinari, and M. C. Righi. Potential energy surface for graphene on graphene: Ab initio derivation, analytical description, and microscopic interpretation. *Phys. Rev. B*, 86:245434, Dec 2012.
- [42] M. Samah, M. Bouguerra, L. Guerbous, and M. Berd. DFT based study of Au_n(4–7) clusters: new stabilized geometries. *Physica Scripta*, 75(4):411–413, feb 2007.

- [43] G. Shafai, S. Hong, M. Bertino, and T. S. Rahman. Effect of ligands on the geometric and electronic structure of Au_{13} clusters. *The Journal of Physical Chemistry C*, 113(28):12072–12078, 2009.
- [44] L. Suzhi, L. Qunyang, W. C. Robert, G. Peter, Z. L. Xin, D. Xiangdong, S. Jun, and L. Ju. The evolving quality of frictional contact with graphene. *Nature*, 539:541–545, 2016.
- [45] T. Thonhauser, V. R. Cooper, S. Li, A. Puzder, P. Hyldgaard, and D. C. Langreth. Van der waals density functional: Self-consistent potential and the nature of the van der waals bond. *Phys. Rev. B*, 76:125112, Sep 2007.
- [46] J. Wang, G. Wang, and J. Zhao. Density-functional study of Au_n ($n=2-20$) clusters: Lowest-energy structures and electronic properties. *Phys. Rev. B*, 66:035418, Jul 2002.
- [47] K. Watanabe, T. Taniguchi, and H. Kanda. Direct-bandgap properties and evidence for ultraviolet lasing of hexagonal boron nitride single crystal. *Nature Materials*, 3:404–409, May 2004.
- [48] M. Wolloch, G. Levita, P. Restuccia, and M. C. Righi. Interfacial charge density and its connection to adhesion and frictional forces. *Phys. Rev. Lett.*, 121:026804, Jul 2018.
- [49] L. Xiao, B. Tollberg, X. Hu, and L. Wang. Structural study of gold clusters. *The Journal of Chemical Physics*, 124(11):114309, 2006.
- [50] Y. Yang and S. Chen. Surface manipulation of the electronic energy of subnanometer-sized gold clusters: an electrochemical and spectroscopic investigation. *Nano Letters*, 3(1):75–79, 2003.
- [51] J. Yin, M. Hu, Z. Yu, C. Zhang, L. Sun, and J. Zhong. Direct or indirect semiconductor: The role of stacking fault in h-BN. *Physica B-condensed Matter*, 406:2293–2297, May 2011.
- [52] J. Zhao, J. Yang, and J. G. Hou. Theoretical study of small two-dimensional gold clusters. *Phys. Rev. B*, 67:085404, Feb 2003.